ACSNANO

www.acsnano.org

ARTICLE

Mitochondrial-Targeted Metal-Phenolic Nanoparticles to Attenuate Intervertebral Disc Degeneration: Alleviating Oxidative Stress and Mitochondrial Dysfunction

Qizhu Chen,[□] Qiuping Qian,[□] Hongbo Xu,[□] Hao Zhou,[□] Linjie Chen, Nannan Shao, Kai Zhang, Tao Chen, Haijun Tian, Zhiguang Zhang, Morgan Jones, Kenny Yat Hong Kwan, Mathew Sewell, Shuying Shen, Xiangyang Wang, Moonis Ali Khan, Pooyan Makvandi, Shengwei Jin,* Yunlong Zhou,* and Aimin Wu*

Cite This: *ACS Nano* 2024, 18, 8885−8905

Read Online

ACCESS | Metrics & More | Article Recommendations | Supporting Information

ABSTRACT: As intervertebral disc degeneration (IVDD) proceeds, the dysfunctional mitochondria disrupt the viability of nucleus pulposus cells, initiating the degradation of the extracellular matrix. To date, there is a lack of effective therapies targeting the mitochondria of nucleus pulposus cells. Here, we synthesized polygallic acid-manganese (PGA-Mn) nanoparticles via self-assembly polymerization of gallic acid in an aqueous medium and introduced a mitochondrial targeting peptide (TP04) onto the nanoparticles using a Schiff base linkage, resulting in PGA-Mn-TP04 nanoparticles. With a size smaller than 50 nm, PGA-Mn-TP04 possesses pH-buffering capacity, avoiding lysosomal confinement and selectively accumulating within mitochondria through electrostatic interactions. The rapid electron exchange between manganese ions and gallic acid enhances the redox capability of PGA-Mn-TP04, effectively reducing mitochondrial damage caused by mitochondrial reactive oxygen species. Moreover, PGA-Mn-TP04 restores mitochondrial function by facilitating the fusion of mitochondria and minimizing their fission, thereby sustaining the vitality of nucleus pulposus cells. In the rat IVDD model, PGA-Mn-TP04 maintained intervertebral disc height and nucleus pulposus tissue hydration. It offers a nonoperative treatment approach for IVDD and other skeletal muscle diseases resulting from mitochondrial dysfunction, presenting an alternative to traditional surgical interventions.

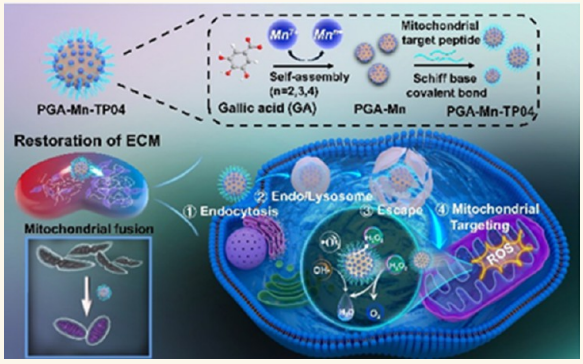

KEYWORDS: *mitochondrial target, mitochondrial dysfunction, metal-phenolic nanoparticles, reactive oxygen species scavenging, intervertebral disc degeneration*

INTRODUCTION

Low back pain (LBP) is a common global public health issue, and with the aging population, the economic burden of LBP has significantly increased.[1,2] According to relevant studies, over 80% of adults will experience LBP at some point in their lives. Approximately 10% of LBP patients will eventually develop into chronic disabilities.[3,4] Therefore, LBP has become one of the major diseases that impacts public health and quality of life.

Although there are various factors contributing to LBP, intervertebral disc degeneration (IVDD) is recognized as one of the major contributors.[5,6] IVDD is characterized by the loss of resident cells and extracellular matrix (ECM).[7] Nucleus pulposus cells (NPCs), the primary cell type in the center of the intervertebral disc (IVD), play a crucial role in producing ECM and maintaining the microenvironment of the IVD.[8−10] It has been demonstrated that during the progression of IVDD, a substantial accumulation of dysfunctional mitochondria

Received: December 4, 2023
Revised: February 28, 2024
Accepted: March 5, 2024
Published: March 11, 2024

https://doi.org/10.1021/acsnano.3c12163
ACS Nano 2024, 18, 8885−8905

Scheme 1. Schematic Representation of the Mechanism by Which Nanoparticles Act inside NPCs

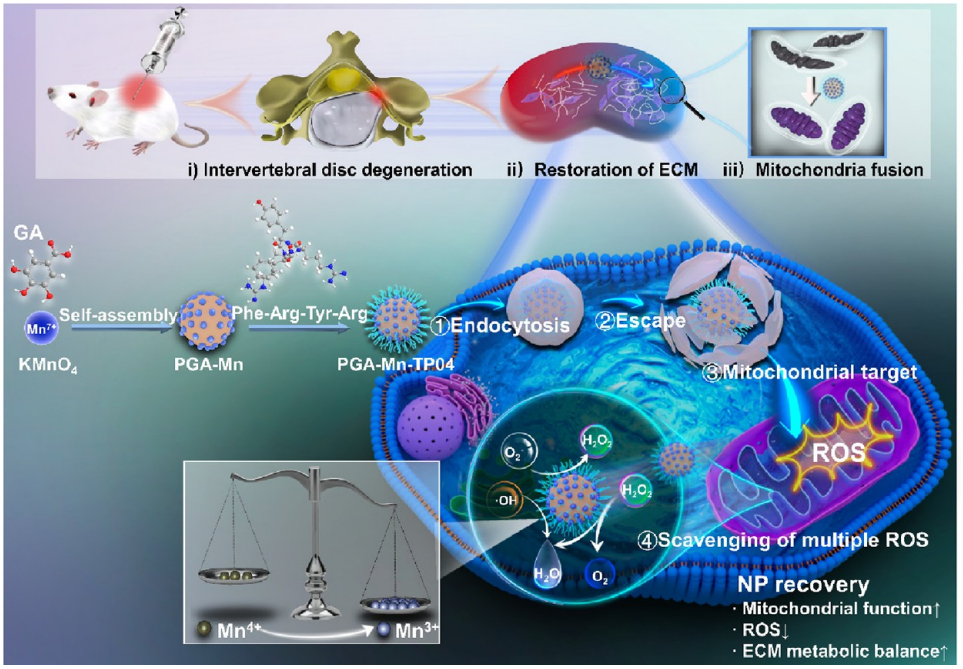

impairs the normal functionality of NPCs. This impairment subsequently leads to the degradation of the ECM, reduction in water content, and depletion of proteoglycan levels within the nucleus pulposus (NP). Ultimately, these cumulative effects contribute to structural alterations in a degenerative cascade and subsequent spinal instability.[11,12] Currently, there is a lack of definitive medications available in clinical practice to directly treat IVDD. As a result, patients primarily rely on nonsteroidal anti-inflammatory drugs and analgesic drugs to alleviate the symptoms.[13] Unfortunately, this symptomatic relief does not restore the normal function of the intervertebral disc and sometimes comes with various side effects.[14] Therefore, the development of more effective treatment strategies is urgently needed, and currently available treatment options include biomaterial replacement,[15] drug injection,[14,16] gene therapy,[17,18] and stem cell therapy.[19] Albeit the precise etiology of IVDD remains elusive, augmentation and rehabilitation of mitochondrial function represent a potential avenue for therapeutic intervention.[11,20]

Mitochondria are crucial organelles in eukaryotic cells. They serve as the primary energy generators, supplying a large portion of the cell's energy needs.[21] In addition to their involvement in energy production, mitochondria actively participate in regulating cellular metabolism and the cell cycle through multiple pathways.[22,23] Therefore, mitochondria are indispensable for maintaining cellular homeostasis and ensuring normal cell function. Furthermore, as highly dynamic organelles, mitochondria maintain a delicate balance between fusion and fission processes under normal physiological conditions.[21,24] However, during the process of IVDD, dysfunctional mitochondria are prone to generate a large number of mitochondrial ROS (mROS), which act as major disruptors of mitochondrial fusion and fission.[25] Excessive production of mROS leads to an increased rate of fission, resulting in mitochondrial fragmentation and insufficient fusion events. As a result, this disruption impairs mitochondrial function, hampers ATP generation, and renders dysfunctional mitochondria more prone to generate reactive oxygen species (ROS), forming a harmful vicious cycle.[26] Ultimately, this process inflicts significant oxidative stress damage on the NPCs, accelerating the degradation of the IVD microenvironment. Therefore, reducing the disruption of mROS on mitochondrial function and restoring mitochondrial function holds great promise for improving IVDD.

Currently, antioxidant agents targeting ROS primarily include small molecule compounds,[27] natural nanoenzymes,[28] and artificial nanomaterials.[29] Compared to small molecule compounds and natural nanoenzymes, artificial nanomaterials exhibit superior stability and efficient, long-lasting activity in clearing multiple types of ROS.[30] Therefore, the advantages of artificial nanomaterials make them a promising approach for nonpharmacological disease treatments. There have been ample reports on the use of artificial nanoenzymes for ROS scavenging in the treatment of IVDD.[31,32] However, during the process of cellular internalization, the large size of artificial nanomaterials poses a challenge for their cellular uptake,[33] and artificial nanomaterials may be recognized as foreign objects by lysosomes and subsequently engulfed, resulting in diminished activity within cells.[34,35] Additionally, the protection and repair of mitochondrial function are crucial aspects that require careful attention. mROS are the main contributor to mitochondrial damage; the limited diffusion radius of mROS (approximately 20 nm) presents a challenge in effectively targeting and clearing ROS in the mitochondrial region, thereby restricting the ability to protect and restore mitochondrial function.[36,37] Currently, most biomaterials designed to target mitochondria are focused on mitochondrial membrane potential, which aims to damage mitochondria rather than repair their function.[38,39] Therefore, in the treatment of IVDD, the design of nanomaterials needs to consider efficient escape from lysosomes following cellular uptake, effective and low-toxicity mitochondrial targeting, and the ability to restore mitochondrial function.

https://doi.org/10.1021/acsnano.3c12163
ACS Nano 2024, 18, 8885−8905

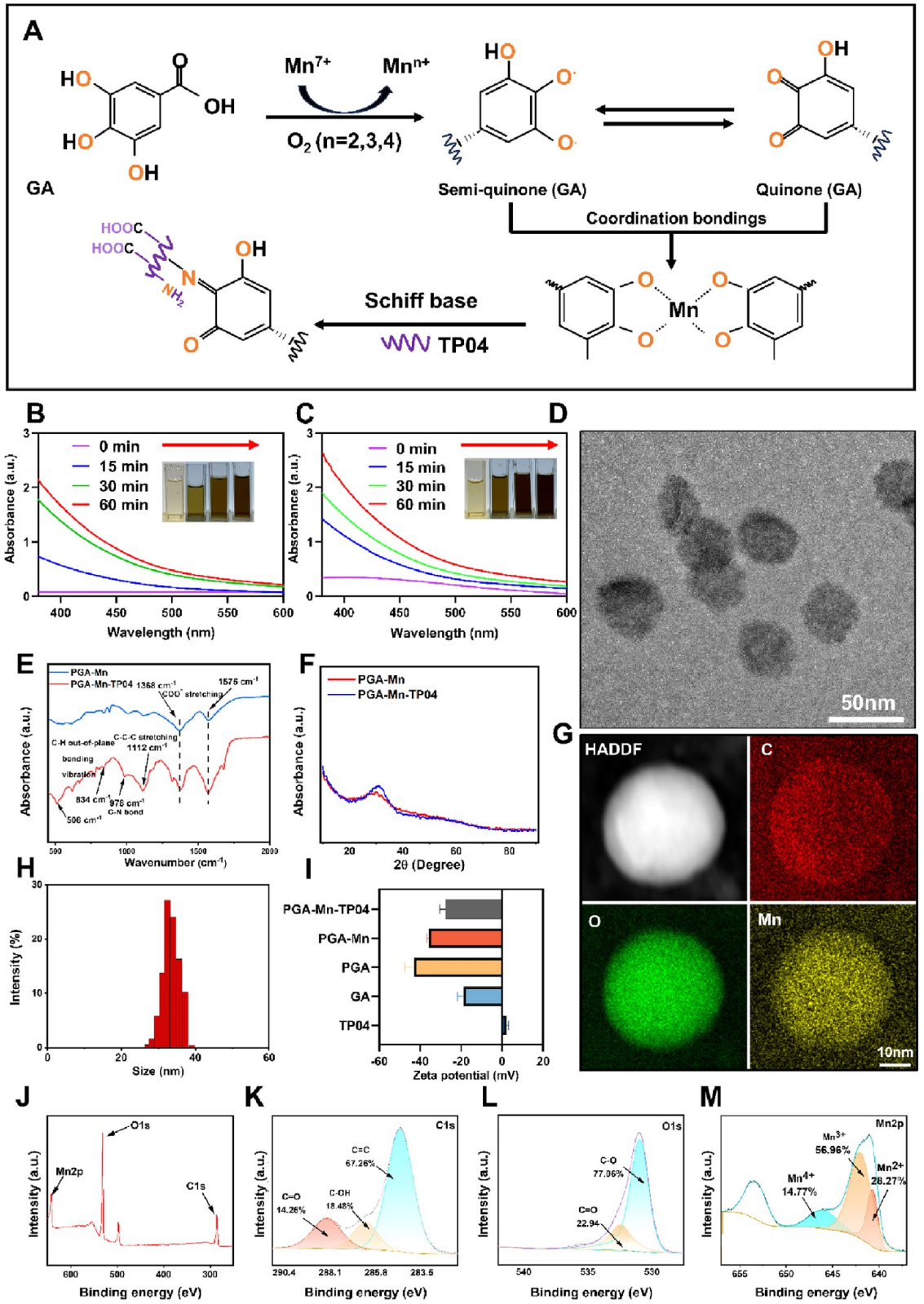

Figure 1. Preparation and characterization of the PGA-Mn-TP04. (A) Schematic representation for the synthesis of the PGA-Mn-TP04. (B,C) UV−vis absorption spectra showing the reaction kinetics of PGA and PGA-Mn polymerization. (D) TEM (n = 3, bar: 50 nm) and (G) corresponding EDX elemental mapping for PGA-Mn-TP04 (n = 3, bar: 10 nm). (E) FTIR spectra and (F) powder X-ray diffraction (XRD) patterns of different materials. (H) Size distribution of PGA-Mn-TP04. (I) Zeta potentials of different materials. (J) Full scan XPS survey spectrum and the high-resolution spectra of PGA-Mn-TP04 for (K) C 1s, (L) O 1s, and (M) Mn 2p.

In this study, we developed antioxidant nanoparticles called polygallate-manganese (PGA-Mn) by combining gallic acid (GA) with manganese ions using a self-assembly method. To enhance their mitochondria-targeting capabilities, we further

https://doi.org/10.1021/acsnano.3c12163
ACS Nano 2024, 18, 8885−8905

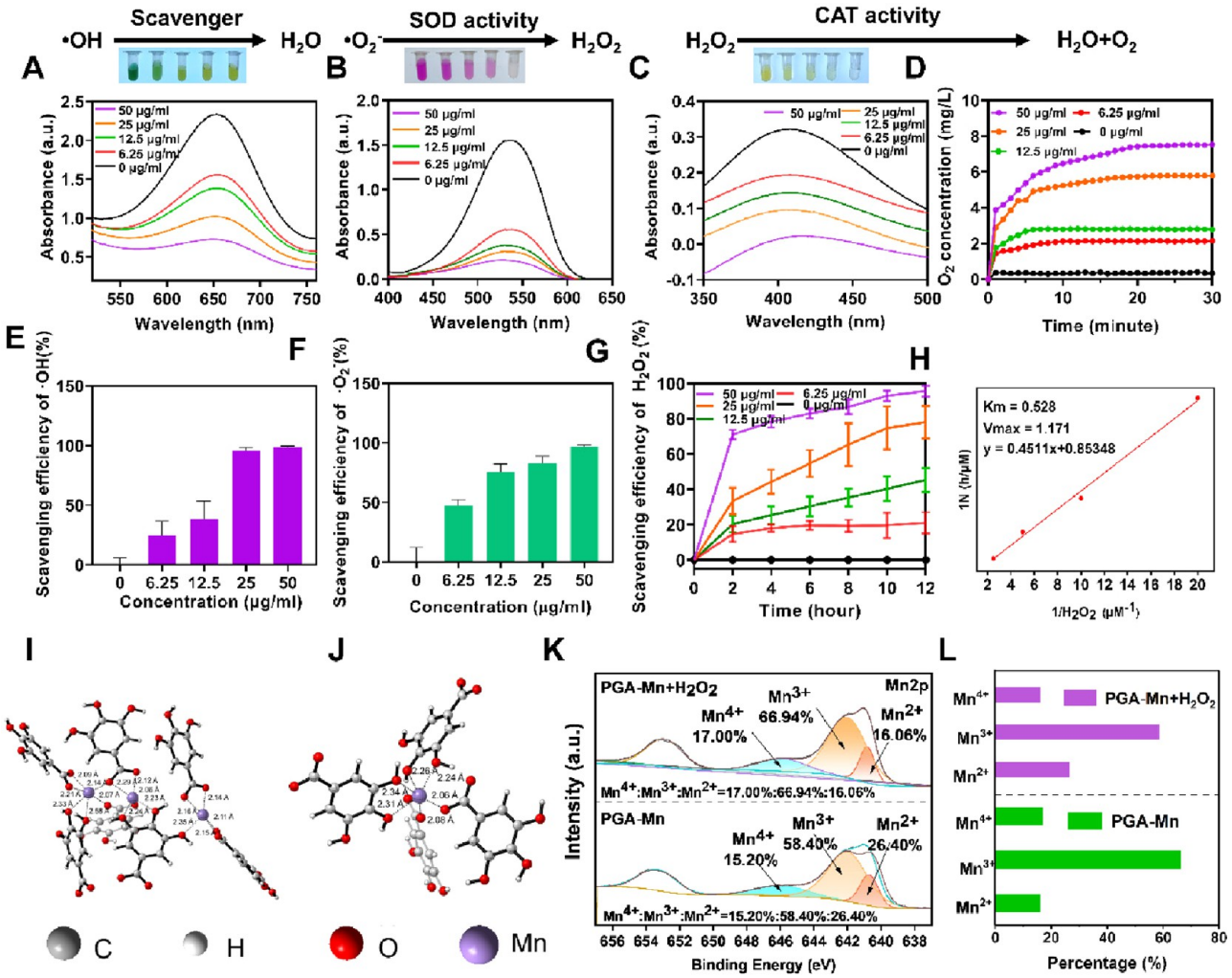

M

$$H_2O_2 \leftrightarrow HO_2^- + H^+ \quad (1)$$

$$nMn^{3+} + nGA \rightarrow [Mn(II)GA^{4-}]_{(x,y,z)}- \quad \iiint dxdydz = n \quad (2)$$

$$[Mn(II)GA^{4-}]_{(x,y,z)}- + HO_2^- \rightarrow [Mn(III)GA\bullet]_{(x,y,z)}- + HO_2^{\bullet} \quad (3)$$

$$HO_2^{\bullet} + H_2O \rightarrow H_3O^+ + O_2^{\bullet -} \quad (4)$$

$$[Mn(III)GA\bullet]_{(x,y,z)}- + H_3O^+ + O_2^{\bullet -} \rightarrow [Mn(II)GA^{4-}]_{(x,y,z)}- + O_2 + OH^- \quad (5)$$

Figure 2. ROS scavenging capacity and mechanism assessment of the PGA-Mn. (A−C) UV−vis absorbance spectra showing the radical eliminating activities of PGA-Mn for (A) ·OH, (B) $\cdot O_2^-$, and (C) H_2O_2 in 0.5 h (n = 3). (D) Real-time O_2 generation curves of the PGA-Mn in H_2O_2 solutions. (E) ·OH and (F) $\cdot O_2^-$ scavenging efficiency of PGA-Mn with various concentrations. (G) H_2O_2 scavenging efficiency at different concentrations of PGA-Mn over time. (H) Double reciprocal plot for PGA-Mn with H_2O_2 as the substrate. (I) Representative trinuclear moder of GA-Mn as well as the distribution of spin density indicating interaction between the Mn center and gallate ligand forming ligand field. (J) Chelation of manganese ion center by four gallate molecules in GA-Mn. (K) XPS high-resolution spectra of the PGA-Mn and H_2O_2 treated PGA-Mn for Mn 2p. (L) Content of various Mn states of the PGA-Mn and H_2O_2 treated PGA-Mn. (M) Proposed chemical reactions for the formation of PGA-Mn.

modified the nanoparticles by attaching a mitochondria-targeting peptide (TP04) through a Schiff base reaction. This resulted in the synthesis of PGA-Mn-TP04 nanoparticles with specific mitochondrial targeting properties. First, the nanoparticles, with a size of less than 50 nm and pH-buffering properties, enable efficient internalization and trigger the "proton sponge effect" to escape from lysosomes after internalization. Second, polyphenols have the potential to repair mitochondrial function,[40] and the electron transfer between polyphenols and metals facilitates the rapid clearance of various ROS, mimicking the activities of superoxide dismutase (SOD) and catalase (CAT). Moreover, the

https://doi.org/10.1021/acsnano.3c12163
ACS Nano 2024, 18, 8885−8905

specifically designed TP04 targeting ligand, with hydrophobic and lipophilic characteristics, ensures successful targeting of mitochondria while maintaining cell viability. This strategy significantly improves mitochondrial function in NPCs, thereby maintaining ECM metabolism balance. The efficacy of PGA-Mn-TP04 has been confirmed in a rat model of IVDD. It has been observed that these nanoparticles effectively maintain disc height, preserve the integrity of the NP structure, and even promote regeneration of the NP tissue. These research findings highlight the potential of PGA-Mn-TP04 as a transformative therapeutic approach, demonstrating tangible benefits in addressing the complex pathogenesis of IVDD. (Scheme 1).

RESULTS AND DISCUSSION

Preparation and Characterization of PGA-Mn-TP04. As an endogenous phenolic compound, gallic acid, devoid of the ester group, can chelate with transition metals, enhancing its antioxidant capacity.[41] Manganese stands as a vital trace element essential for the human body, primarily serving as an activator for various enzymes.[42] Of particular significance is its role as a catalyst for superoxide dismutase (Mn-SOD) within mitochondria.[43] Taking into consideration the presence of manganese ions in mitochondrial SOD enzyme, we opt for manganese ion coordination with GA.

PGA-Mn was facilely prepared via polymerization of GA under an aqueous solution, followed by a self-assembly process (Figure 1A). The synthesis condition is rather mild (10 mM PBS, pH 7.4) owing to Mn^{7+} catalysis. The generation of PGA-Mn can be easily monitored by UV−vis spectra with a rapid increase of absorbance from 400 to 800 nm, accompanied by the darkened color of the reaction solution (Figure 1C). With the aid of Mn^{7+}, the reaction can finish in 1 h, while the polymerization reaction was relatively slow in the absence of Mn^{7+} (Figure 1B). Mn^{7+} has strong oxidation, while GA has reducing properties. The Mn^{7+} catalyzes the REDOX polymerization reaction of GA to generate o-quinone derivatives, which are further polymerized to form dimers and polymers. Gel permeation chromatography (GPC) spectra of the product before (~170) and after (~1493) polymerization show the average molecular weight, which further confirms the success of PGA-Mn polymerization (Table S4). In addition, to enhance the mitochondria-targeting and biocompatibility ability of PGA-Mn, TP04, composed of Phe-Arg-Tyr-Arg, was chemically modified onto the nanoparticles through Schiff base bonding. The PGA-Mn-TP04 are nanoparticles, which have spherical morphology based on both SEM and TEM microscopies (Figures 1D and S1). The average size is about 38.06 nm. From elemental mapping images, the nanoparticles were mainly composed of C, O, and Mn elements, owing to coordination between the Mn ion and surface abundant oxygen groups of PGA (Figure 1G). Fourier transform infrared spectroscopy (FTIR) was further performed to confirm that PGA-Mn-TP04 included the main characteristic peaks of both GA and TP04. The absence of the typical carboxylic acid carbonyl stretch C=O vibration, typically intense in the 1760−1690 cm^{-1} interval, implies the presence of two bands resonating at 1550 and 1368 cm^{-1} due to COO^- stretching. This confirms that PGA-Mn-TP04 is exclusively polyanionic, with the vasC=C fundamental vibration of the aromatic ring appearing overlapped with the vas(COO^-) stretch bands. Additional assignments include C−C−C stretching at 1112 cm^{-1} and the C−N bond at 978 cm^{-1}. A notable C−H(−N=C−H) out-of-plane bending vibration emerges at 834 cm^{-1}, along with a characteristic absorption peak at 508 cm^{-1}. Collectively, these spectral features suggest that PGA-Mn has successfully undergone a reaction with TP04, forming a Schiff's base (Figures 1E and S2), and most of the characteristic peaks of X-ray diffraction analysis (XRD) of GA disappear (Figures 1F and S3), likely due to the oxidative polymerization of GA. Meanwhile, X-ray photoelectron spectroscopy (XPS) was further performed to explore the surface composition, and a full scan spectrum confirmed that the PGA-Mn-TP04 mainly consisted of elements of carbon, oxygen, and manganese, as shown in Figures 1J and S4. From high-resolution C 1s XPS spectra, four peaks were observed at 284.6, 286.4, and 288.3, which can be ascribed to C=C (67.26%), C−OH (18.48%), and C=O (14.26%) species, respectively (Figure 1K). The O 1s XPS spectrum showed two peaks at 532.4 and 530.8 eV (Figure 1L), which belonged to the C=O and C−O bonds, respectively. The Mn 2p XPS spectra are obtained by Gaussian curve-fitting. In Figure 1M, three peaks at 640.6, 642.2, and 646.1 eV indicated that Mn existed in the form of Mn^{2+}−Mn^{4+} on the PGA-Mn-TP04. Meanwhile, the ratio of Mn^{3+} to Mn^{2+} was about 56.96:28.27. To further quantify the Mn amount, PGA-Mn-TP04 was pretreated with aqua regia for ICP-MS analysis, and Mn content accounted for 10.80% total mass of the nanoparticles, verifying the effective removal of Mn ions (Table S1). These data indicated that Mn metals tend to coordinate with polyphenols (PGA) to form metal-phenolic networks. The dynamic light scattering (DLS) of PGA-Mn-TP04 showed a hydrodynamic size of 38.06 ± 2.6 nm in water (Figure 1H), and the zeta potential of PGA-Mn-TP04 (−28 ± 2.82 mV) was much higher than PGA (−46.21 mV), due to TP04 (the positive zeta potential is 2.3 ± 0.56 mV) fully fixed on the PGA-Mn (Figure 1I and Table S2). Meanwhile, PGA-Mn-TP04 maintains excellent stability (Figure S5), which ensures a reliable foundation for subsequent biological application.

ROS Scavenging Capacity and Mechanism Assessment of the PGA-Mn. The development of IVDD is closely related to persistent high levels of ROS, and therefore, the scavenging of excess ROS is of crucial importance to delay IVDD. ROS mainly contain ·OH, $\cdot O_2^-$, and H_2O_2, and we mainly discuss the scavenging of these three types of ROS by PGA-Mn.

·OH can degrade DNA and cell membranes, which is the most destructive ROS.[44] As shown in Figure S6A, the order of ·OH clearance at 50 μg/mL by different materials was PGA-Mn > GA > PGA. In addition, PGA-Mn showed extremely high sensitivity to ·OH. The absorbance of ·OH at 652 nm decreased with increasing PGA-Mn concentration, and ·OH clearance reached 95.43% at 25 μg/mL (Figure 2A,E). It can be concluded that PGA-Mn has a powerful scavenging effect on OH•.

The intracellular antioxidant process first begins with SOD dismutation, which converts $\cdot O_2^-$ to H_2O_2 and O_2. Therefore, we first examined the SOD enzyme activity of PGA-Mn. Superoxide anion reacts with hydroxylamine hydrochloride to form NO_2^-, and NO_2^- in the presence of *p*-aminobenzenesulfonamide and naphthalene ethylenediamine hydrochloride generates violet-red azo compounds with a characteristic absorption peak at 530 nm. Therefore, we detected the SOD enzyme mimetic activity of PGA-Mn for superoxide anion scavenging by UV spectrophotometer absorption at 530 nm. As shown in Figure S6B, the ability of PGA-Mn to remove

https://doi.org/10.1021/acsnano.3c12163
ACS Nano 2024, 18, 8885−8905

$\cdot O_2^-$ was stronger than that of PGA and GA. The absorbance of $\cdot O_2^-$ at 532 nm decreased with the concentration of PGA-Mn (Figure 2B). At concentrations greater than 25 μg/mL, PGA-Mn almost completely removed $\cdot O_2^-$ (Figure 2F). This is because the SOD mimetic activity of PAG-Mn leads to $\cdot O_2^-$-disproportion. Due to the multivalent change of Mn, $\cdot O_2^-$ is reduced to H_2O_2 by the high-valence Mn and oxidized to O_2 by the low-valence Mn, and the valence switch (Mn high-valence/Mn low-valence state) is accelerated by GA.

The dismutation of $\cdot O_2^-$ produces H_2O_2, which can be further decomposed into harmless H_2O and O_2 through the CAT mimetic activity of PGA-Mn. We examined the scavenging efficiency of PGA-Mn on H_2O_2 by detecting the characteristic peak at 410 nm produced by the reaction of $Ti(SO_4)_2$ with H_2O_2. The results of the study demonstrated that PGA-Mn exhibited the most potent scavenging effect on H_2O_2, and this effect was further enhanced with increasing concentrations of PGA-Mn. Specifically, when the concentration of PGA-Mn reached 50 μg/mL, approximately 66% of the H_2O_2 was effectively removed, leading to the release of a significant amount of O_2. This release of O_2 was visually evident as bubbles that could be observed within the test tube. These findings indicate the strong antioxidant capabilities of PGA-Mn and its potential in scavenging H_2O_2 (Figures 2C,D and S6C). To evaluate the catalytic activity of PGA-Mn, we further investigated the steady-state catalytic kinetics to calculate the steady-state kinetic parameters. These include the Michaelis constant (K_m) and the maximum initial velocity (V_{max}). For the CAT mimetic activity, the Km of PGA-Mn was 0.53 μM, and the V_{max} was 1.171 M/h (Figure 2H). This indicates that PGA-Mn has a high affinity for H_2O_2, and it can react rapidly with H_2O_2 produced. In summary, our findings reveal that polymerized and coordinated gallic acid with Mn significantly enhances its antioxidant capacity. Moreover, PGA-Mn demonstrates an effective ability to scavenge various ROS.

Ligand-Field-Enhanced Chemical Reactions. To investigate the scavenging properties of the GA-Mn complex on ROS (H_2O_2), it is essential to gain a comprehensive understanding of the coordination chemistry between GA-Mn and the functionalities of the ligand field that regulate chemical reactions. Therefore, density functional theory (DFT) calculations were carried out to mimic the binding interaction of Mn(III) and gallic acid in complexes. The analysis of the potential stable coordination structure (Mn(III) and gallic acid in the ratio of 1:4 or 3:7) reveals that the coordination process involves carboxylate and ortho-position phenol groups, acting as bridge ligands connecting the manganese ion center. The complex structures were optimized with B3LYP method 1−3 with 6-31G(d) 4 basis set for C, H, O elements and the LANL2DZ 5 basis set for Mn (III). The benzoate oxygen in the two gallate molecules and the ortho-phenolic group in the two gallate molecules are chelated with a manganese ion. Density functional theory (DFT) calculations indicate that the binding energy (ΔG) between manganese ions and GA is approximately 186.54 kcal/mol (Figures 2I and S8). Meanwhile, it is noteworthy that DFT calculations suggest the spin density of the GA-Mn complex is primarily concentrated on the manganese center, with secondary localization on the bonded phenolic and carboxylate oxygens. The pseudoradical electronic structure of gallate facilitates the reduction of ligands and metals, leading to the adoption of a high-spin state by the manganese center (Figures 2J and S9). In the trinuclear complex of manganese ions and GA, the lower binding energy of a single manganese ion to GA is about −175.88 kcal/mol, indicating a promising redox performance of the Mn centers as active sites. The surrounding ligand field functions as a potential guide for electrons, facilitating their movement and supporting the catalytic decomposition of H_2O_2 on the metal sites.

Molecular-orbital theory elucidates that, during the coordination reaction forming the GA-Mn complex,[45−50] the interaction between the d (t_{2g}) orbital function of Mn^{3+} and the π-orbital function of gallate results in the creation of two new molecular orbital functions: a low-energy bonding orbital function (t_{2g}) and a high-energy antibonding orbital function (t_{2g}*) (Figure S10). Fortunately, the energy level of the gallate ligand's π-orbital is lower than that of the d orbital of Mn^{3+}, leading to an abundance of delocalized unpaired electrons in the gallate. Consequently, the electrons of the π-orbital of the ligand occupy the newly formed t_{2g} bonding orbital, while the electrons of the d orbital of Mn^{3+} occupy the t_{2g}* antibonding orbital. This positions gallate as an electron donor, facilitating reduction reactions on the Mn centers while the ligand itself undergoes oxidation, assisted by the metal center acting as an electron transporter. Abdel-Hamid et al. proposed the oxidation mechanism of gallate (GA^{4-}), involving its first one-electron oxidation, resulting in the formation of the semiquinone radical ($GA^{\cdot 3-}$).[51,52] These oxidation processes of gallate are irreversible, indicating continuous decay of the ligand field during the redox reaction of the Mn center. Building upon previous research on the oxygen-reduction capability of iron-polyphenol complexes,[46,53] we initially inferred a sequential redox catalytic mechanism triggered by the GA-Mn complex.[54,55] In this mechanism (Figures 2M and S10), the gallate ligand plays a crucial role by first facilitating the one-electron reduction of an Mn (III) center to Mn (II). Subsequently, the electron is transferred to produce. Under the action of $\cdot O_2^-$, Mn (III) is regenerated, thereby providing more catalytically active sites for hydrogen peroxide decomposition, ultimately leading to the production of O_2. In addition, in our experimental tests, it was observed that the GA-Mn complex rapidly produces oxygen upon contact with hydrogen peroxide, whereas the reaction efficiency of PGA alone is noticeably low. This observation supports the validity of our inference.

In addition, after GA-Mn catalyzes the decomposition of hydrogen peroxide, the proportion of corresponding trivalent manganese increases, which can be seen from Mn 2p XPS data in Figures 2K,L and S11. This sequence behavior of the manganese ion supports the gallate-Mn-oxygen electron flux, which involves intermolecular electron transfer and gain/loss in the gallate ligand. This, in turn, ensures the availability of more active sites for metal coordination. Overall, the proposed mechanism highlights the crucial role of gallate in enabling redox reactions of the Mn center and underscores the continuous cycling of manganese ions to sustain the catalytic process. This unique interplay between gallate, Mn ions, and oxygen species enhances the electron transfer within the GA-Mn complex, ensuring a higher density of active sites for effective metal coordination. It is anticipated that PGA-Mn exhibits stronger hydrogen peroxide scavenging properties in experimental results. The unique interplay between the gallate ligand and the Mn center, along with the availability of more catalytically active sites, suggests that PGA-Mn would be more efficient in neutralizing hydrogen peroxide and scavenging ROS like H_2O_2. Moreover, in situ electrochemical tests

https://doi.org/10.1021/acsnano.3c12163
ACS Nano 2024, 18, 8885−8905

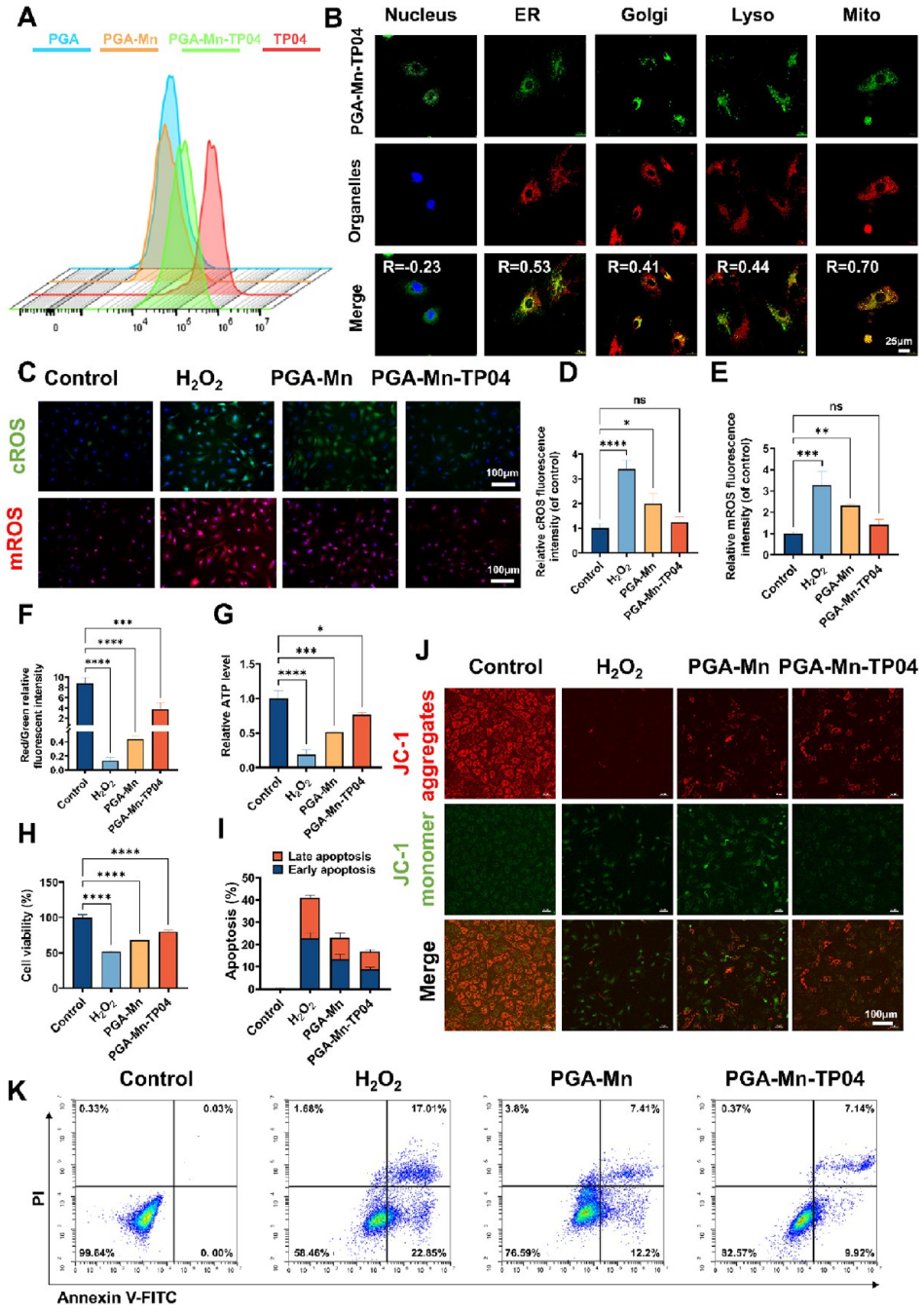

Figure 3. PGA-Mn-TP04 inhibits apoptosis by scavenging ROS. (A) Evaluation of the binding ability of different materials labeled with FITC to mitochondria. Separated mitochondria were incubated with various materials labeled with FITC at 37 °C for 1 h. The fluorescence of the mitochondrial suspension was measured using a flow cytometer (n = 3). (B) Cell nuclei, mitochondria, Golgi apparatus, lysosome, endoplasmic reticulum, and PGA-Mn-TP04 were stained by the DAPI, Mito-Tracker Red, Golgi-Tracker green, Lyso-Tracker green, ER-Tracker Green, and PGA-Mn-TP04-FITC; CLSM images of colocalization of PGA-Mn-TP04 with different organelles (n = 3). (C) Representative cROS (green fluorescence) and mROS staining (red fluorescence) of NPCs under different treatment conditions (n = 3). (D,E) Quantitative analysis of cROS and mROS levels in NPCs under different treatment conditions. (F) Quantitative analysis of JC-1 levels in NPCs under different treatment conditions. (G) Relative ATP amount in NPCs under different treatments (n = 3). (H) Cell viability of NPCs in different treatment conditions (n = 3). (I) Quantitative analysis of early apoptotic and late apoptotic cell ratios in NPCs under different treatment conditions. (J) Representative fluorescent images of JC-1 staining under different treatment conditions (n = 3). (K) Flow cytometry apoptosis analysis of NPCs under different treatment conditions (n = 3). (ns. no significant difference, ****p < 0.0001, ***p < 0.001, **p < 0.01, *p < 0.05 as compared with the control group.).

analyzing the PGA-Mn and ROS processes reveal similar phenomena, further confirming PGA-Mn's role as a catalyst for H_2O_2 decomposition by promoting cycling between Mn^{2+} and Mn^{3+} (Figure S12). We also employed GPC to assess the molecular weight changes before and after the reaction between PGA-Mn and H_2O_2. The results indicated a decrease in the molecular weight of PGA-Mn upon exposure to H_2O_2 (Table S4). In summary, the results from the experiments and the underlying mechanism demonstrate the potent capability of PGA-Mn in effectively eliminating ROS.

https://doi.org/10.1021/acsnano.3c12163
ACS Nano 2024, 18, 8885−8905

Endocytosis, Lysosomal Escape, and Mitochondrial Targeting of PGA-Mn-TP04. To enhance the cellular uptake and targeting of PGA-Mn to mitochondria, we implemented a modification of TP04 on PGA-Mn. The cytotoxicity of PGA-Mn and PGA-Mn-TP04 was evaluated using the CCK8 method and hemolysis test, and it was observed that both nanoparticles maintained a high cell viability within the tested concentration range; we selected 50 μg/mL as the safest dose for subsequent studies (Figures S13 and S14). In addition to assessing cytotoxicity, efficient cellular internalization and lysosomal escape are crucial for targeted nanoparticle delivery to the mitochondria.[56] To visualize cellular internalization and lysosomal escape, FITC-labeled PGA-Mn and PGA-Mn-TP04 were employed. Compared to PGA-Mn, PGA-Mn-TP04 demonstrated significantly higher cellular uptake efficiency (Figure. S15). The results can be attributed to the surface modification of PGA-Mn-TP04 with TP04, resulting in a positively charged surface. This positive charge has a strong affinity for negatively charged cells, facilitating their cellular uptake compared to unmodified PGA-Mn.

Previous studies have shown that nanoparticles with pH-buffering properties promote the influx of hydrogen ions, chloride ions, and water into endocytosed vesicles before acidification and fusion with lysosomes. This sequential process leads to endosomal rupture and prevents the degradation of metal-polyphenol nanoparticles by lysosomes.[57,58] The coordination between PGA and manganese ions contributes to increased flexibility and pH-buffering capability in the PGA-Mn structure. As depicted in Figure S16, the pH-buffering effect of PGA-Mn was found to be stronger compared to PGA, allowing it to buffer hydrogen ions within endocytic vesicles and promote the influx of water. PGA-Mn exhibits a stronger pH-buffering capacity, primarily due to its rich concentration of carboxyl groups. These groups engage in coordination with manganese ions, consequently influencing the ionization equilibrium of water molecules. Moreover, some carboxyl groups dissociated from PGA-Mn in the endosome confer it with endosomal escape capability. The pH-buffering characteristic leads to endosomal rupture and prevents lysosomal hydrolysis.[59] Additionally, the colocalization experiment with lysosomes demonstrated that PGA-Mn possessed enhanced escape ability (Figure S17). The affinity for mitochondria is crucial in targeting mitochondria. Hence, we labeled different materials with FITC and coincubated them with free mitochondria at 37 °C for 1 h. The binding ability between different materials and mitochondria was quantitatively analyzed using flow cytometry. As shown in Figure 3A, the affinity of PGA-Mn-TP04 and TP04 toward mitochondria is significantly higher than that of PGA-Mn and PGA. Subsequently, we examined the localization of PGA-Mn modified by TP04 within intracellular organelles to determine its ability to selectively target mitochondria following lysosomal escape. To achieve this, we labeled PGA-Mn-TP04 with FITC and used different probes to label major intracellular organelles. The degree of colocalization between PGA-Mn-TP04 and individual organelles was quantified using Pearson's *R*-value, which ranges from −1 (indicating a negative correlation) to +1 (indicating a positive correlation). The results demonstrated a significant overlap between the fluorescence signal of PGA-Mn-TP04 and mitochondria, which was higher compared to other organelles (Figure. 3B). Additionally, under TEM electron microscopy, we observed concurrent localization of PGA-Mn-TP04 close to the mitochondria (Figure S18). In contrast, the targeting ability of PGA-Mn was greatly reduced without the modification of TP04 (Figure S19). The outcomes observed can be attributed to the alternating arrangement of aromatic and basic amino acids in TP04, which imparts hydrophobic and lipophilic properties to the compound. This characteristic enables PGA-Mn-TP04 to selectively target mitochondria through electrostatic adsorption, irrespective of the membrane potential at the mitochondrial surface.

PGA-Mn-TP04 Inhibits Apoptosis by Scavenging ROS. To elucidate the potential cellular protective mechanism of PGA-Mn-TP04, NPCs were exposed to 100 μM H_2O_2 for 6 h to induce oxidative stress. Subsequently, PGA-Mn and PGA-Mn-TP04 were administered to evaluate their intracellular antioxidant effects. Mito-SOX and DCFH-DA fluorescent dyes were employed for the detection of mitochondrial ROS (mROS) and cytosolic ROS (cROS), respectively (Figure 3C). In the H_2O_2 group, both cROS and mROS levels significantly increased compared to the control group. The fluorescence intensity of cROS and mROS in the PGA-Mn group was approximately 50 and 70% of that in the H_2O_2 group, respectively. Notably, the PGA-Mn-TP04 group exhibited substantially lower fluorescence intensity, with only 36% for cROS and 43% for mROS, compared to the H_2O_2 group (Figure 3D,E). Moreover, as the concentration of PGA-Mn-TP04 increases, its efficacy in clearing both mROS and cROS also improves (Figure S20). These observations provide evidence that PGA-Mn possesses an excellent ability to scavenge reactive oxygen species (ROS) not only extracellularly but also within the biological system. Moreover, the scavenging efficacy of PGA-Mn-TP04 is notably enhanced following the modification with a mitochondrial targeting peptide. The reason behind this lies in the fact that ROS are mainly generated within the mitochondria.[9] By leveraging its mitochondrial targeting properties, PGA-Mn-TP04 effectively eliminates ROS at their point of origin, thereby preventing their extensive propagation within cells.

Excessive ROS can disrupt mitochondrial membrane potential, leading to mitochondrial membrane depolarization ($\Delta\Psi$m) and subsequent dysfunction.[60] The control group exhibited a high red/green fluorescence ratio, indicative of normal $\Delta\Psi$m. In contrast, the H_2O_2 group displayed a significant decrease in the red/green fluorescence ratio, reflecting $\Delta\Psi$m depolarization. Both the PGA-Mn and PGA-Mn-TP04 groups exhibited partial improvement in the red/green fluorescence ratio, with the PGA-Mn-TP04 group showing superior improvement (Figure 3F,J). Considering that mitochondrial ATP production relies on the $\Delta\Psi$m generated by proton pumps,[61] we further examined the ATP production ability of NPCs in each experimental group. In the H_2O_2 group, NPCs displayed only 18.96% of the ATP production compared to the control group, implying a significant impact of oxidative stress on oxidative phosphorylation. However, the ATP production in the PGA-Mn group was partially restored to 51.21% of the control level, and in the PGA-Mn-TP04 group, ATP production was further restored to 76.50% of the control level (Figure 3G). These findings highlight the ability of PGA-Mn-TP04 to maintain mitochondrial membrane potential and restore ATP production in NPCs suggesting its potential to protect mitochondria from oxidative damage and preserve their proper functioning.

As ROS plays a crucial role in the development of cellular apoptosis,[62] we also assessed the impact of different treatments

https://doi.org/10.1021/acsnano.3c12163
ACS Nano 2024, 18, 8885−8905

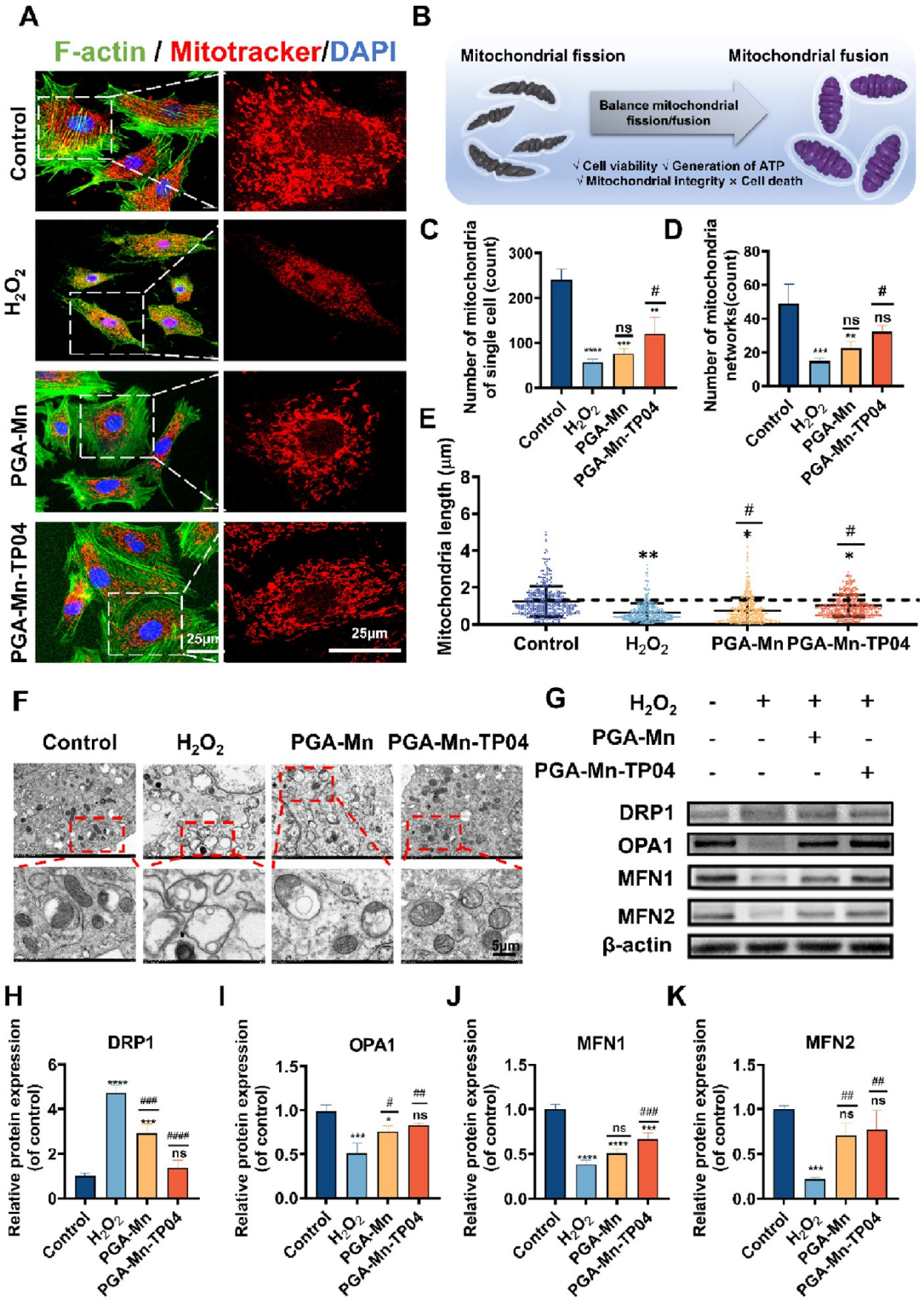

Figure 4. Effect of PGA-Mn-TP04 on correcting the balance of mitochondrial fusion and fission. (A) Representative images of distribution and status of mitochondria in NPCs after different treatments (n = 3). (B) Schematic illustration of PGA-Mn-TP04 correcting the balance of mitochondrial fusion and fission. (C−E) ImageJ analysis of the number of mitochondria, network, and mitochondrial length. (F) TEM images of mitochondria in NPCs under different treatment conditions (n = 3). (G−K) Western blot analysis and semiquantification of mitochondrial fusion and fission related proteins (n = 3). (ns. no significant difference, ****p < 0.0001, ***p < 0.001, **p < 0.01, *p < 0.05 as compared with the control group; ####p < 0.0001, ###p < 0.001, ##p < 0.01, #p < 0.05 as compared with the H_2O_2 group).

on apoptosis using flow cytometry. In Figure 3I,K, the H_2O_2 group exhibited a significantly higher apoptosis rate compared to the control group. Notably, PGA-Mn-TP04 demonstrated a more pronounced inhibition of apoptosis compared to the PGA-Mn group, indicating its stronger protective effect against oxidative stress. These findings were further supported by cell viability analysis using CCK8, which confirmed that PGA-Mn-TP04 completely protected the cells from the detrimental

https://doi.org/10.1021/acsnano.3c12163
ACS Nano 2024, 18, 8885−8905

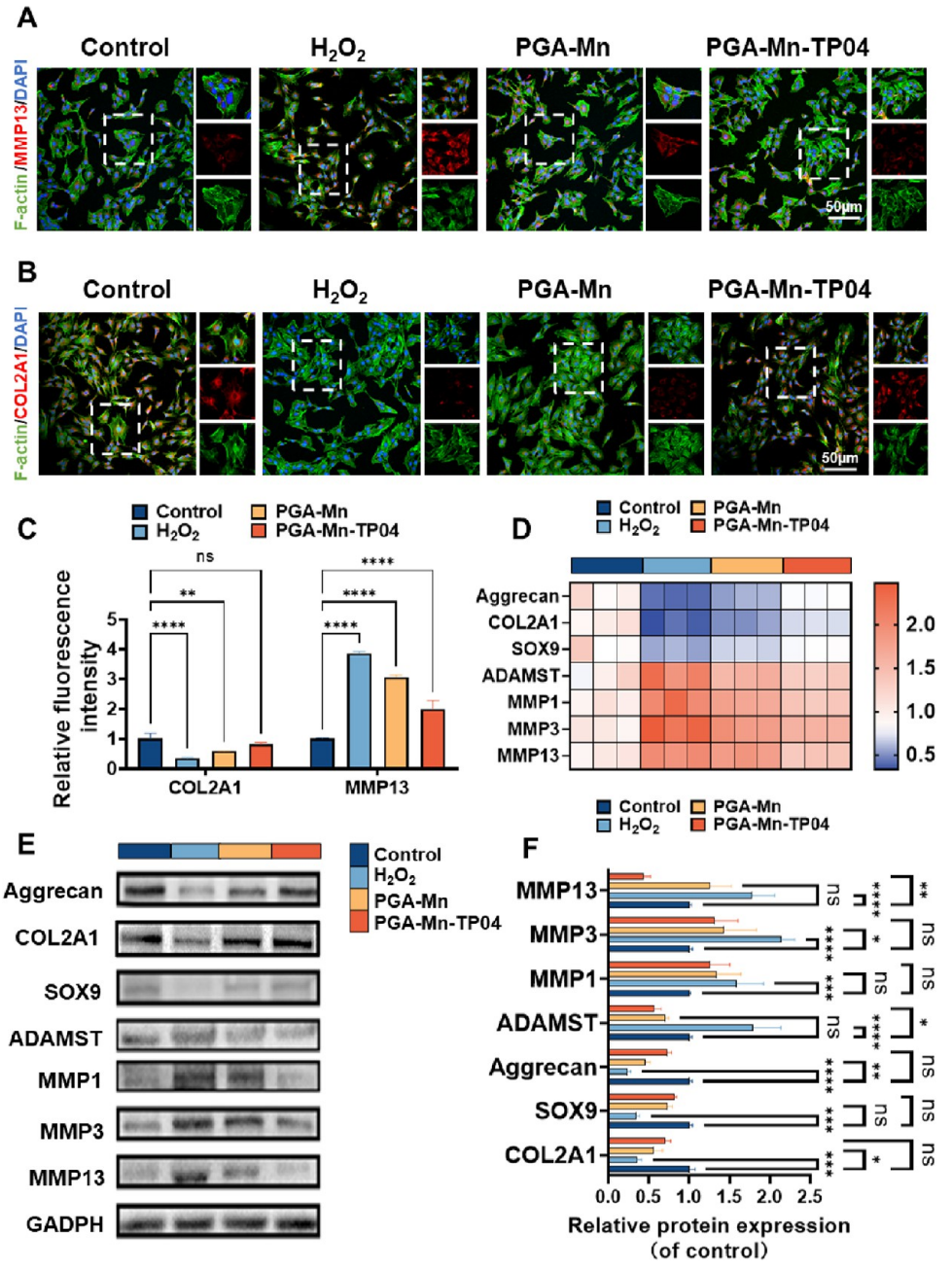

Figure 5. PGA-Mn-TP04 maintains the balance of ECM anabolism and catabolism. (A,B) Immunofluorescence staining of MMP13, COL2A1 in NPCs (n = 3, bar: 50 μm). (C) Their semiquantitative analysis of fluorescence intensity (n = 3). (D) The relative mRNA expressions of MMP1, MMP3, MMP13, Aggrecan, COL2A1, and SOX-9 (n = 3). (E,F) Western blot analysis and semiquantification of MMP1, MMP3, MMP13, ADAMST, Aggrecan, COL2A1, and SOX-9 (n = 3). (ns. no significant difference, ****p < 0.0001, ***p < 0.001, **p < 0.01, *p < 0.05 as compared with the control group).

effects of 100 μM H_2O_2, a concentration higher than that found in the classical pathological microenvironment of IVDD (Figure 3H). Taken together, the results highlight the therapeutic potential of PGA-Mn-TP04 in treating degenerative disc diseases associated with oxidative stress-induced mitochondrial dysfunction in NPCs.

PGA-Mn-TP04 Restored Mitochondrial Function by Promoting Mitochondrial Fusion. Mitochondria are highly susceptible to the interference of ROS, resulting in an imbalance between fusion and fission processes, often leading to an increase in mitochondrial fission events.[24] The balance between fusion and fission is critical for the normal functioning of mitochondria and plays a crucial role in the viability of NPCs (Figure 4B).[12,21]

To examine whether the protective effects of different materials are associated with mitochondrial fusion and fission, NPCs were cultured under various treatment conditions. Mitochondria in NPCs were labeled using Mito-Tracker, a mitochondrial dye, enabling a more intuitive visualization of mitochondrial morphology and size using confocal microscopy. The images were then analyzed using ImageJ software (Figure 4A,C−E). Mitochondria can form networks within the cell that are tightly integrated with other cellular compartments.[63] In the control group, the number of mitochondrial network of

https://doi.org/10.1021/acsnano.3c12163
ACS Nano 2024, 18, 8885−8905

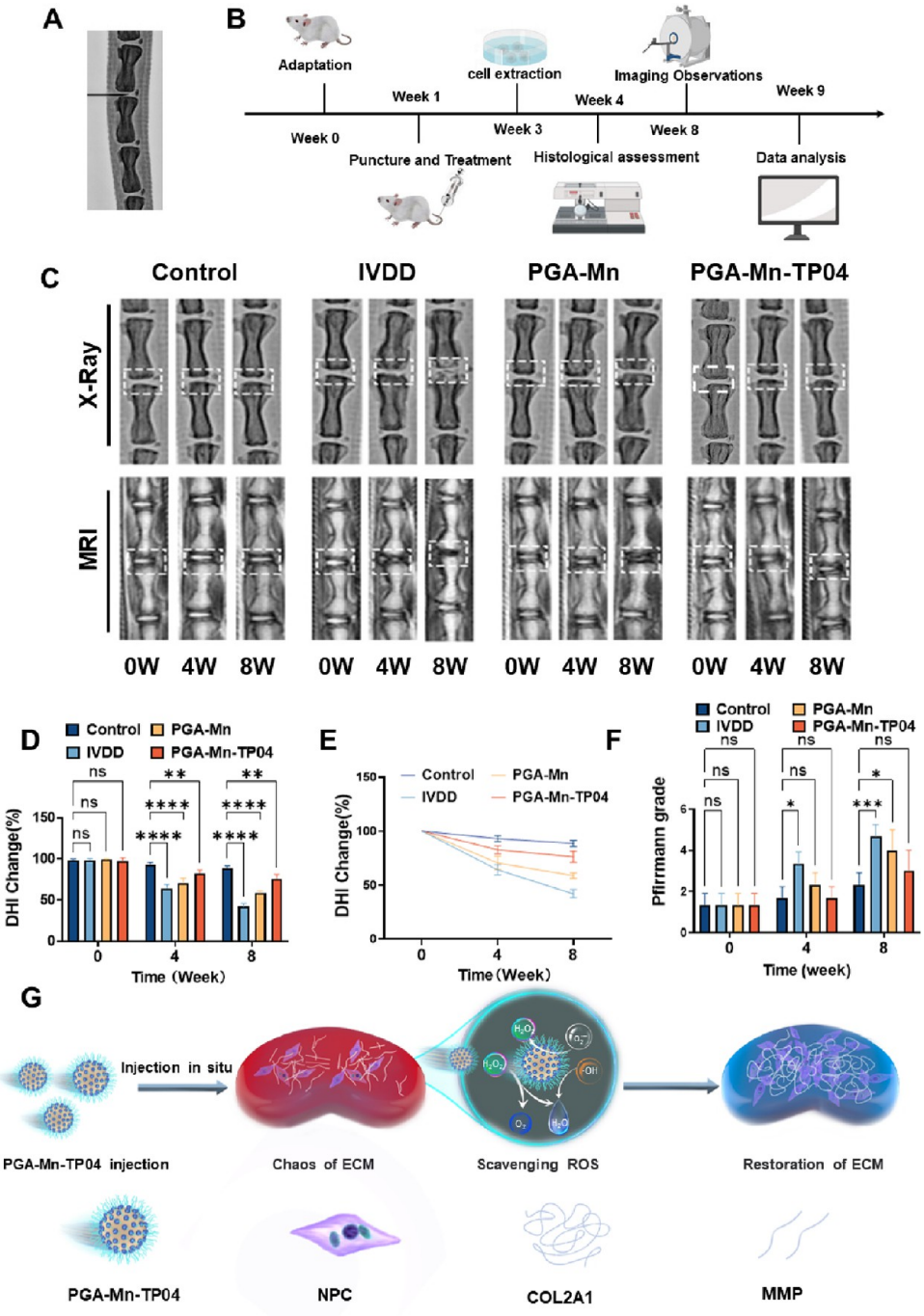

Figure 6. PGA-Mn-TP04 rescues IVDD after acupuncture surgery in rats. (A) Acupuncture model of rat. (B) Schematic illustration of animal experiments. (C) X-ray and MRI images of rat coccygeal vertebrae after different treatments. (D,E) DHI changes in different groups from 0 to 8 weeks after surgery (n = 3). (F) Pfirrmann grade changes of different groups from 0 to 8 weeks after surgery. (G) Schematic illustration on PGA-Mn-TP04 restoring ECM. (ns. no significant difference, ****p < 0.0001, ***p < 0.001, **p < 0.01, *p < 0.05 as compared with the control group).

NPCs was 48, of which the number of mitochondria was 240, and the average length of mitochondria was 1.25 μm. However, due to the interference of oxidative stress, the average length of mitochondria in the H_2O_2 group was only half of that in the control group, and the mitochondrial network was significantly reduced. However, their number is not increased by mitochondrial fission, which is due to autophagy of dysfunctional mitochondria damaged by oxidative stress, a protective mechanism designed to remove damaged or nonfunctional mitochondria. Both the mitochondrial network and the number of mitochondria were increased in the PGA-Mn and PGA-Mn-TP04 groups, and the mitochondrial length was also restored. The effect of PGA-Mn-TP04 on mitochondria was more obvious.

To further demonstrate that PGA-Mn-TP04 can regulate mitochondrial fission and fusion, we examined the expression levels of several proteins related to mitochondrial fission and fusion by Western blot (Figure 4G). Among them, dynamin-related protein 1 (Drp1) is a fission-related protein, and optic atrophy 1 (OPA1) and mitofusin 1/2 (Mfn1/2) are fusion-

https://doi.org/10.1021/acsnano.3c12163
ACS Nano 2024, 18, 8885−8905

related proteins. Compared to the control group, the expression of Drp1 was upregulated, while the expression of OPA1 and Mfn1/2 was decreased in the H_2O_2 group. This indicates an increase in mitochondrial fission and a decrease in fusion. However, the administration of PGA-Mn and PGA-Mn-TP04 reversed these effects. In particular, the PGA-Mn-TP04 group restored the balance between mitochondrial fission and fusion (Figure 4H−K).

To gain direct insight into the changes in mitochondrial morphology following damage, transmission electron microscopy (TEM) was employed (Figure 4F). In the control group, mitochondria exhibited rod-shaped and elongated morphology with prominent mitochondrial cristae, resembling healthy mitochondrial morphology.[64] Conversely, the mitochondria in the H_2O_2 group displayed notable swelling and some even appeared ruptured. Treatment with PGA-Mn and PGA-Mn-TP04 reduced mitochondrial swelling and rupture, particularly in the PGA-Mn-TP04 group. Due to the excellent mitochondrial targeting effect of PGA-Mn-TP04, mitochondria were protected against oxidative stress-induced damage, maintained a healthy morphology, and retained intact mitochondrial cristae. Overall, these results indicate that the accumulation of PGA-Mn-TP04 in NPCs helps maintain the balance between mitochondrial fusion and fission, ultimately restoring healthy mitochondrial morphology.

PGA-Mn-TP04 Maintained ECM Metabolic Balance. The ECM is primarily composed of polymeric proteins secreted by NPCs, with proteoglycans and collagen being the main components. The ECM connects with Aggrecan via filamentous collagen fibers of COL2A1, forming a network structure. This structure plays a vital role in water retention in the NP tissue and imparts unique mechanical properties to the IVD. SOX-9, a protein that promotes cartilage development, is an essential component involved in the repair of ECM, thus delaying intervertebral disc degeneration IVDD.[65] Currently, existing research has demonstrated that an excess of ROS can induce the overproduction of hydrolases in NPCs by modulating the epigenetics of NPCs and activating the cGAS-Sting axis.[66,67] Under the interference of ROS, NPCs produce a large number of matrix metalloproteinases (MMPs) and proteoglycans, such as ADAMTS. These hydrolases cause significant damage to the ECM structure, leading to the loss of original mechanical properties in the NP tissue and the acceleration of IVDD. To assess the effects of different treatments on ECM-related gene and protein expression, we employed Western blotting, quantitative PCR (qPCR), and immunofluorescence techniques.

In Figure 5A,B, compared to the control group, the fluorescence intensity of COL2A1 and Aggrecan significantly decreased, while the fluorescence intensity of MMP3 and MMP13 significantly increased under H_2O_2 stimulation, indicating a decrease in ECM synthesis. However, in comparison to the H_2O_2 group, the expressions of COL2A1 were increased, and the expressions of MMP13 were decreased in the PGA-Mn and PGA-Mn-TP04 groups (Figure 5C). These findings suggest that PGA-Mn and PGA-Mn-TP04 can effectively counteract the ECM remodeling induced by oxidative stress. To further verify these findings, we conducted Western blot analysis (Figure 5E,F) and qPCR analysis (Figure 5D). The results at the protein level aligned with the gene expression level. Compared to the control group, the H_2O_2 group exhibited upregulated protein and mRNA expressions of MMP1, MMP3, MMP13, and ADAMTS5, while the protein and mRNA expressions of COL2A1, Aggrecan, and SOX-9 were downregulated. These findings further confirm the detrimental effects of oxidative stress on the ECM. Importantly, the PGA-Mn and PGA-Mn-TP04 groups showed decreased expression of ECM degradation proteases and increased expression of COL2A1, Aggrecan, and SOX9, with PGA-Mn-TP04 exhibiting the most significant reversal of ECM destruction under oxidative stress. These results indicate that PGA-Mn-TP04 can modulate the expression of these proteases, thereby promoting the synthesis of the extracellular matrix during oxidative stress-induced remodeling.

Imaging Evaluation of the Therapeutic Efficacy of PGA-Mn-TP04 in Vivo. To assess the efficacy of the different materials in ameliorating IVDD, we created an IVDD model in Sprague−Dawley (SD) rats using acupuncture, as depicted in Figures 6A and S21. Based on the data from the hemolysis assay and CCK-8 (Figures S13 and S14), we chose 50 μg/mL as the safe concentration for injection. Next, the various materials were injected in situ. Imaging techniques were employed at 0, 4, and 8 weeks to observe the degeneration of IVDs in each group, and histological sections were collected for analysis (Figure 6B). The live imaging analysis reveals that PGA-Mn-TP04 predominantly resides within the intervertebral disc following in situ injection, with a sustained presence lasting for 13 days (Figure S22). The percentage of disc height index (DHI) and the degree of IVDD were evaluated using X-ray and magnetic resonance imaging (MRI) scans, according to the Pfirrmann classification system (Figure S23). These assessments were carried out to determine the impact of the different treatments on IVDD progression and to gauge the efficacy of the materials in mitigating degenerative changes in IVDs.

As shown in Figure 6C, the qualitative analysis of X-ray images revealed significant decreases in DHI in the IVDD group compared to the control group. Additionally, noticeable osteophyte formation was observed on both sides of the disc above and below the cone. The PGA-Mn group showed a partial reduction in disc height, indicating a limited effect on delaying disc degeneration. On the other hand, the PGA-Mn-TP04 group exhibited the lowest decrease in DHI, which closely resembled the control group, with preserved disc height. MRI is considered the gold standard for IVDD diagnosis. In healthy IVDs, hydrated NP tissue can be visualized on MRI as hyperintensity on T2-weighted images. However, during the process of disc degeneration, the remodeling of ECM leads to decreased water content and volume, resulting in the appearance of "black discs" on MRI scans when degeneration is severe.[68] The MRI images showed that the control group exhibited healthy IVDs, with similar signal intensities observed in the PGA-Mn-TP04 group. Conversely, most IVDs in the IVDD group lost their signals, and "black discs" were evident. The signal intensities of IVDs in the PGA-Mn group were slightly higher than those in the IVDD group but lower than those in the PGA-Mn-TP04 group. The changes in DHI and MRI grades were consistent and supported the potential of PGA-Mn-TP04 in ameliorating IVDD in vivo (Figure 6D−F). In summary, these results suggest that PGA-Mn-TP04 has the potential to ameliorate IVDD by protecting the NP tissue and maintaining disc height (Figure 6G).

Histology Evaluation of the Therapeutic Efficacy of PGA-Mn-TP04 in Vivo. Furthermore, these findings were further supported by histological analysis of the IVD.

https://doi.org/10.1021/acsnano.3c12163
ACS Nano 2024, 18, 8885−8905

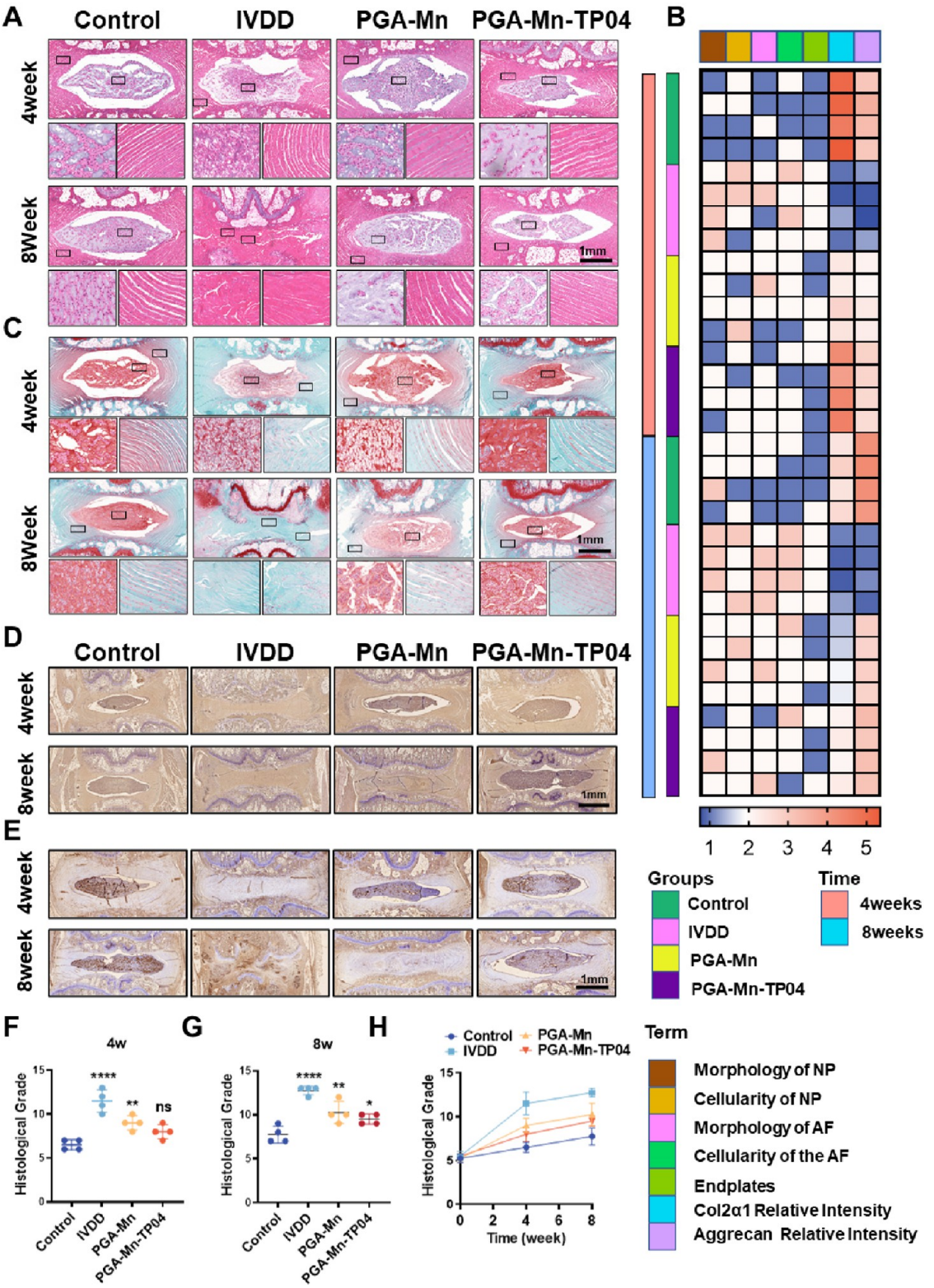

Figure 7. Histological data of animal experiments. (A) HE staining images of IVD at 4 and 8 weeks after surgery (n = 4, bar: 1 mm). (B) Heatmap of variables of histological scoring and IHC relative staining intensity at 4 and 8 weeks. (C) Safranin-O/Fast Green staining of different groups at 4 and 8 weeks. (D) IHC of COL2A1 and (E) Aggrecan at 4 and 8 weeks after surgery (n = 4, bar: 1 mm). (F,G) Histological grades at 4 and 8 weeks after surgery (n = 4, bar: 1 mm). (H) Histological grade changes after surgery (n = 4). (ns. no significant difference, ****p < 0.0001, ***p < 0.001, **p < 0.01, *p < 0.05 as compared with control the group).

Hematoxylin and eosin (H&E) staining was performed to observe the cellular structure and morphology of the NP, annulus fibrosus (AF), and end plate (Figure 7A). From 4 to 8 weeks, a significant decrease in the number of NPCs was observed in the IVDD group. The NP area gradually underwent replacement by fibroblasts, and the annulus fibrosus

https://doi.org/10.1021/acsnano.3c12163
ACS Nano 2024, 18, 8885−8905

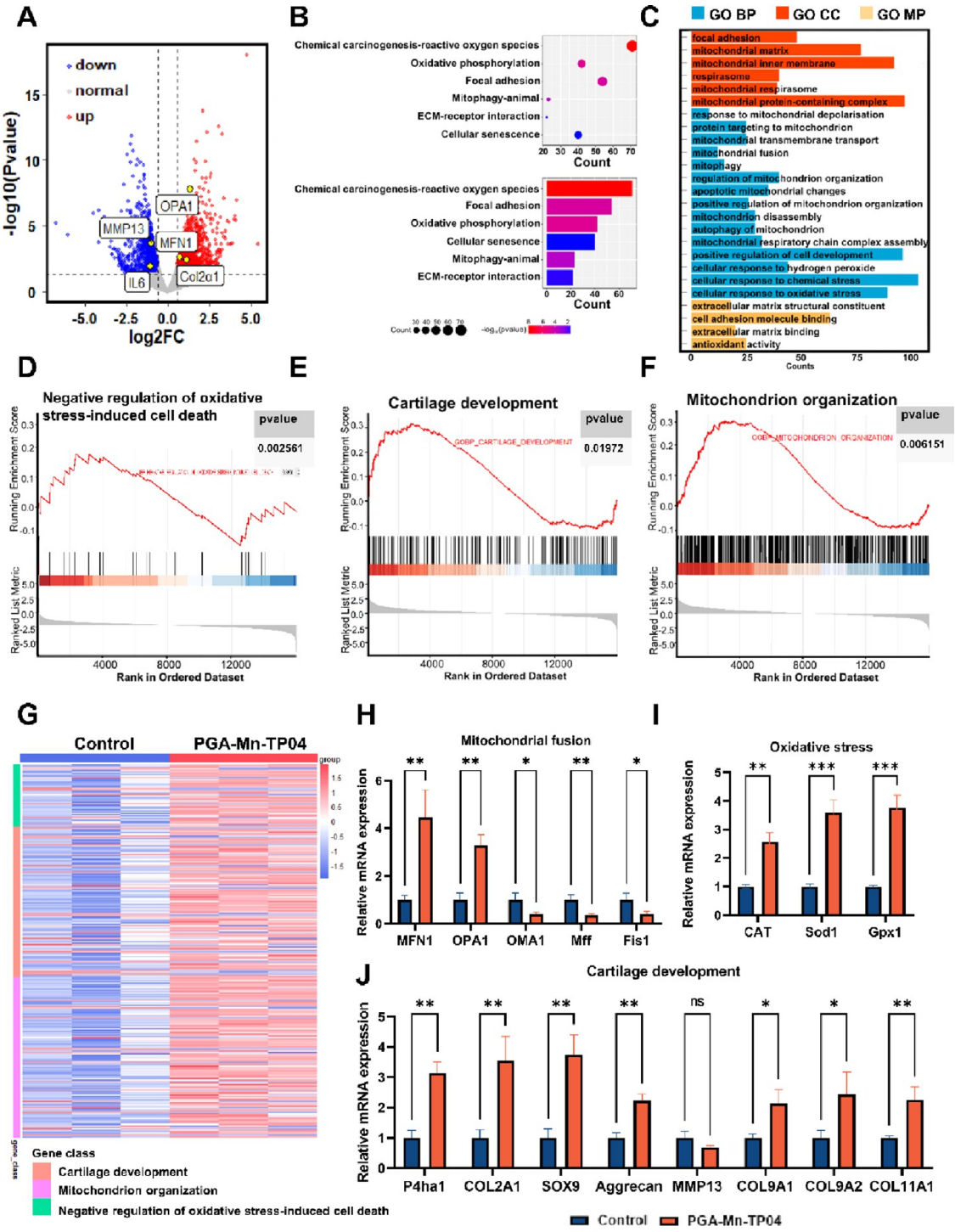

Figure 8. Therapeutic mechanisms of PGA-Mn-TP04 on IVDD. (A) Volcano plots showing the identified upregulated and downregulated genes by PGA-Mn-TP04. (B) KEGG pathway enrichment analysis. (C) GO pathway enrichment analysis. (D−F) GSEA enrichment analysis of negative regulation of oxidative stress-induced cell death (p = 0.002561), cartilage development (p = 0.0192), and mitochondrial organization (p = 0.006151) between the control and PGA-Mn-TP04 groups. (G) Heatmap of genes related to negative regulation of oxidative stress-induced cell death, mitochondrial organization, and cartilage development in the control and PGA-Mn-TP04 groups. n = 3. (H−J) qRT-PCR analysis of genes associated with oxidative stress, mitochondrial fusion, and cartilage development. (n = 3). (p < 0.01, *p < 0.05 as compared with the control group).**

and cartilage end plate exhibited increasing fractures. In the PGA-Mn group, there was a reduction in NPCs, and the border between the AF and NP was disrupted. However, in the PGA-Mn-TP04 group, there was only a slight alteration in the NPC population, with no significant difference compared to the control group. The tissue margins were clearly defined, and the AF and cartilage end plate appeared healthy. The staining of Safranin-O/Fast Green was employed to assess the collagen content in the IVD. Proteoglycans are visualized as reddish-brown, while collagen appears blue-green (Figure 7C).

https://doi.org/10.1021/acsnano.3c12163
ACS Nano 2024, 18, 8885−8905

Compared to the control group, the red NP tissue was significantly reduced and replaced by blue fibrous tissue in the IVDD group. The treatment with PGA-Mn resulted in a deceleration of NP degeneration, with substantial preservation of the NP tissue. The PGA-Mn-TP04 group exhibited no significant changes in proteoglycan and collagen content in the NP, as compared to the control group. The tissue scores, as shown in Figure 7F−H, were significantly higher in the IVDD group at 4 and 8 weeks postsurgery, indicating rapid disease progression. Conversely, both PGA-Mn and PGA-Mn-TP04 treatments demonstrated a slower reduction in histological scores, with the PGA-Mn-TP04 group showing the closest resemblance to the control group. Collectively, these histological findings further support the potential of PGA-Mn-TP04 in ameliorating IVDD. The treatment was able to slow down the degeneration process, preserve NP tissue, and maintain tissue structure, as evidenced by the observed cellular morphology, NP preservation, collagen content, and histological scores. Furthermore, cellular inflammation and cell death were assessed using HE staining in key organs including the heart, liver, spleen, lungs, and kidneys. The findings revealed that both PGA-Mn and PGA-Mn-TP04 exhibited excellent biocompatibility, with no apparent toxicity observed in any of the vital organs (Figure S24).

To further illustrate the effectiveness of PGA-Mn-TP04 in promoting ECM synthesis, immunohistochemical (IHC) analysis was conducted to measure the levels of Aggrecan and COL2A1 in the NP tissue (Figure 7D,E). Following the surgical procedures, the yellow color representing Aggrecan and COL2A1 positivity gradually faded in each group. The fading was most pronounced in the IVDD group, where Aggrecan and COL2A1 were predominantly blue, indicating a lack of positivity, after 8 weeks. In comparison, the PGA-Mn group exhibited a slightly higher rate of IHC positivity than the IVDD group, suggesting partial preservation of Aggrecan and COL2A1 expression. Notably, the PGA-Mn-TP04 group displayed the closest rate of IHC positivity to the control group, indicating significant preservation of Aggrecan and COL2A1 levels in the NP tissue. In conclusion, the findings from HE staining, Safranin-O/Fast Green staining, and IHC analysis provide comprehensive evidence of improved IVD morphology, enhanced cartilage distribution, and higher expression of matrix proteins following PGA-Mn-TP04 injection (Figure 7B). This supports the notion that PGA-Mn-TP04 treatment promotes ECM synthesis in the NP tissue, ultimately contributing to the amelioration of IVDD.

Therapeutic Mechanisms of PGA-Mn-TP04 on IVDD. To gain further insights into the mechanism underlying the effects of PGA-Mn-TP04 on NPCs, we conducted mRNA sequencing analysis on NPCs treated with PGA-Mn-TP04. In comparison to the control group, PGA-Mn-TP04 treatment resulted in the upregulation of 1943 genes and the downregulation of 1901 genes ($P < 0.05$, fold change >1.5) (Figure 8A). Gene ontology (GO) pathway enrichment analysis revealed that several pathways, such as focal adhesion, mitochondrial matrix, mitochondrial fusion, and ECM structural constituent, were closely associated with the therapeutic mechanism of PGA-Mn-TP04 (Figure 8C). Moreover, the Kyoto Encyclopedia of Genes and Genomes (KEGG) enrichment analysis demonstrated that pathways related to ROS, oxidative phosphorylation, and focal adhesion were significantly enriched in the PGA-Mn-TP04 group (Figure 8B). Additionally, KEGG pathway analysis indicated that the differentially expressed genes (DEGs) in the PGA-Mn-TP04 group were also enriched in signaling pathways associated with mitophagy, ECM-receptor interaction, and cellular senescence. These findings suggest that PGA-Mn-TP04 treatment influences gene expression patterns in NPCs, potentially modulating processes related to cellular adhesion, mitochondrial function, ECM regulation, ROS, and cellular aging. This comprehensive mRNA sequencing analysis provides valuable information regarding the molecular mechanisms by which PGA-Mn-TP04 exerts its therapeutic effects on IVDD.

PGA-Mn-TP04 treatment can upregulate the negative regulation of oxidative stress-induced cell death to resist oxidative stress damage, as indicated by GSEA analysis (Figure 8D). Furthermore, PGA-Mn-TP04 promotes mitochondrial fusion and increases oxidative phosphorylation levels, suggesting its potential to reduce ROS-induced cell damage and restore mitochondrial function (Figure 8E). During the progression of IVDD, the deterioration of the NP, a soft tissue within the IVD, plays a crucial role in destabilizing the disc structure and accelerating the degenerative process.[8,9] Encouragingly, PGA-Mn-TP04 treatment can delay IVDD by activating cartilage development pathways and promoting NP tissue synthesis (Figure 8F). More specifically, analysis concentrating on mitochondrial organization, negative regulation of oxidative stress-induced cells, and cartilage development demonstrated an upregulation of gene expression associated with these processes after treatment with PGA-Mn-TP04 (Figure 8G). Furthermore, a protein−protein interaction network analysis was performed, highlighting key neighbor proteins connected to leading proteins such as CAT, SOD1, MFN1, OPA1, COL2A1, and Sox9, among others. These genes play important roles in mitochondrial fusion, negative regulation of oxidative stress-induced cells, and cartilage development after PGA-Mn-TP04 treatment (Figure S25A). The evaluation of these key genes revealed upregulation of genes associated with ROS scavenging, suggesting that PGA-Mn-TP04 not only scavenges ROS but also activates the expression of endogenous antioxidant genes in cells. In addition, genes related to antioxidant stress, mitochondrial fusion, and cartilage development are also upregulated after PGA-Mn-TP04 treatment, consistent with the above findings (Figures 8H−J and S26). Furthermore, an intersection analysis of negative regulation of oxidative stress-induced cells, mitochondrial fusion, and cartilage development indicates some shared functional pathways (Figure S25B).

In the RNA-seq analysis described above, it is worth noting that the PGA-Mn-TP04 group was not exposed to H_2O_2. Therefore, the observed positive effects of PGA-Mn-TP04 are most likely due to its direct regulation of cellular genes, rather than any additional effect of PGA-Mn-TP04 on scavenging ROS. In summary, the results provide evidence that PGA-Mn-TP04 can upregulate the expression of antioxidant enzymes in cells, induce mitochondrial fusion, and restore mitochondrial function. These processes contribute to the regeneration of the NP tissue in IVDD.

CONCLUSION

In summary, we designed mitochondria-targeting PGA-Mn-TP04 nanoparticles through the self-assembly of GA and manganese ions. The PGA-Mn-TP04 nanoparticles demonstrated the capability to effectively scavenge multiple mROS and restore the mitochondrial function after targeting the

https://doi.org/10.1021/acsnano.3c12163
ACS Nano 2024, 18, 8885−8905

mitochondria, thereby decreasing oxidative stress in NPCs. In vivo, our studies demonstrated the ability to promote ECM synthesis, maintain disc height, and preserve structural integrity, leading to a delay in disc degeneration. We believe that the preparation of mitochondria-targeting nanoparticles represents a promising strategy for the treatment of IVDD and holds potential for advancements in the treatment of LBP. The results of this study lay the groundwork for future research on the use of antioxidant nanoparticles for treating skeletal muscle diseases associated with mitochondrial dysfunction.

MATERIALS AND METHODS

Preparation of TP04. Solid-phase synthesis of short peptides is a widely used method for constructing polypeptide chains by sequentially adding amino acid residues to a solid support. Here are the general steps involved in solid-phase synthesis of short peptides: **1.** Solid-phase attachment: The reaction vessel is loaded with 200 mg of 2-CTC resin and 2 mL of anhydrous dichloromethane (DCF) to immobilize the solid-phase resin and establish a reaction platform. **2.** Protecting group addition: A solution containing 209.2 g of L-Fmoc-Phe, 2 mL of anhydrous DCF, and 0.54 mL of N, N-diisopropylethylamine (DIEA) is added to the reaction column. The mixture is allowed to react at room temperature for 3 h. After the reaction, the solid phase is washed three times with 5 mL of anhydrous DMF. This step adds a Fmoc protecting group to the solid support, shielding the amino acids during subsequent reactions. **3.** Activation and coupling: The appropriate amino acid residues (e.g., Arg-Tyr-Arg) are coupled to the solid support using an activator and condensation mixture HOBU/HBTU/DIEA in a ratio (3:3:3:6). For example, the amounts used for tyrosine would be 492.6 mg, 146 mg, 410 mg, and 0.36 mL, respectively, while arginine would require 350 mg, 73 mg, 203 mg, and 0.18 mL. This step enhances the efficiency of coupling reactions between amino acids and the active hydroxyl groups on the solid-phase resin. **4.** Elution: Unreacted substances such as unconjugated amino acids, protective groups, and excess activators are removed by washing the solid support with anhydrous DCF and filtration. **5.** Repeated cycles: The above steps are repeated, with amino acid residues being added in sequence to elongate the polypeptide chain until the desired tetrapeptide is obtained. **6.** Deprotection: Excess protecting groups are removed from the polypeptide chain using trifluoroacetic acid (TFA) as a deprotective agent. **7.** Purification: The peptide is purified by adding anhydrous diethyl ether and centrifuging the supernatant 2−3 times to eliminate impurities. The centrifuged precipitate is dissolved in methanol and then lyophilized to obtain a powdered form suitable for further analysis, such as mass spectrometry and HPLC separation and purification. (Table S1)

Preparation of PGA-Mn and PGA-Mn-TP04. First, 0.17 g GA and 0.125 g sodium dodecyl sulfate were dissolved in a mixed solvent (20 mL PBS and 25 mL ethanol). Then, 5 mL $KMnO_4$ solution (6.32 μg/mL) and 1 mL NaOH (1 mM) were added to the solution in sequence. Then mixed solution was stirred mildly at room temperature for 1 h. Finally, the solution was centrifugated at high speed and washed three times with distilled water and ethanol, respectively. The solution was vacuum-dried and dried to obtain PGA-Mn powder.

PGA-Mn and TP04 were dissolved in distilled water at a mass ratio of 5:1 and stirred at a constant speed for 6 h. The uncoupled TP04 was removed by washing three times with distilled water and ethanol. Finally, the solution was vacuum-dried and dried to obtain PGA-Mn-TP04 powder.

To determine the final binding rate of TP04 with PGA-Mn, TP04 was labeled with FITC fluorescence molecules. After the binding process, the characteristic absorption peak at 446 nm was measured using a UV spectrophotometer. The FITC-labeled TP04, with a mass of n_1, was then combined with PGA-Mn of mass N as previously described. Subsequently, the mixture underwent washing and centrifugation using absolute alcohol. The resulting supernatant was collected, and the mass of unbound TP04 (n_2) was calculated by measuring the absorbance at 446 nm in the supernatant (Figure S27).

$$\text{Binding rate}(\%) = \frac{n_1 - n_2}{N} \times 100\%$$

$$\text{Binding rate}(\%) = \frac{5000 - 1309}{25\,000} \times 100\% = 14.8\%$$

H_2O_2 Scavenging Activity. The H_2O_2 solution (800 μM) was mixed with different materials and incubated for 0.5, 1, 2, 4, 8, 12, and 24 h. Then, $TiSO_4$ (1 mg/mL) was added and reacted for 5 min. The absorbance of the obtained solution was 410 nm.

·OH Scavenging Activity. ·OH scavenging activity assay was performed by TMB chromogenic test. The generation of ·OH by the classical Fenton reaction between H_2O_2 and $FeSO_4$ can convert TMB to oxidized TMB (oxTMB) with characteristic absorption at 652 nm. Therefore, the concentration of residual ·OH can be determined by monitoring the absorption at 652 nm. Working test solutions containing 250 μm TMB, 2 mM H_2O_2, 1 mM $FeSO_4$, and various concentrations of PGA-Mn were prepared in PBS buffer (pH = 5.0) in the dark for 5 min. Then, the absorbance peak of the 652 nm solution was monitored by UV−vis spectroscopy.

$\cdot O_2^-$ Scavenging Activity. Superoxide anion reacts with hydroxylamine hydrochloride to form NO_2^-, NO_2^- in the presence of *p*-aminobenzenesulfonamide and naphthalene ethylenediamine hydrochloride forms a purplish-red azo compound with a characteristic absorption peak at 530 nm, and the $\cdot O_2^-$ content in the sample can be calculated from the A530 value. According to the reagent manufacturer's instructions (Solarbio, China), the sample was gradually reacted with reagents I, II, III, and IV in the kit. Finally, the absorbance was observed at 530 nm using UV−vis.

O_2 Generation Activity. To measure the O_2 generating capacity of PGA-Mn, H_2O_2 (1 M) was mixed with different concentrations of PGA-Mn in 10 mL of ddH_2O. O_2 concentrations were then recorded every 1 min using an oxygen dissolvator (JPBJ610L, Shanghai).

Computational Details. Density functional theory (DFT) calculations were carried out to mimic the binding interaction of Mn (III) and gallic acid in complexes in the ratio of 1:4 or 3:7. The complex structures were optimized with B3LYP method[69−71] with the 6-31G(d)[72] basis set for C, H, O elements and the LANL2DZ[73] basis set for Mn(III). The frequency analyses were carried out at the same theoretical level to verify the structures were at a local minimum. The solvent effects were also considered by calculating single point energy using the B3LYP method, the 6-311++G(d, p)[74] basis set for C, H, and O elements, the SDD[75] basis set for Mn element, and the PCM[76] solvation model on the optimized structure. Hirshfeld electron spin density analysis was carried out with Multiwfn software.[77] All the calculations were performed with *Gaussian 09* software.[78] The 3D molecule structures were drawn with *CYLview* (www.cylview.org).[79]

Cell Culture. NP tissues were obtained from Sprague−Dawley rats and incubated with 2 mg/mL collagenase II for 2 h at 37 °C. The collagenase was then removed by centrifugation, and NPCs were cultured in DMEM/F12 with 10% fetal bovine serum (Gibco, USA), 100 U mL^{-1} penicillin, and 100 μg mL^{-1} streptomycin. The cells were cultured in a 37 °C incubator in an atmosphere containing 5% CO_2. The culture medium was refreshed every 2 days.

In Vitro Mitochondrial Targeting Validation. According to the instructions of the mitochondrial isolation kit, the NPCs were gathered and homogenized mechanically, and then, the mitochondria were separated after centrifugation. Next, the mitochondria were coincubated with FITC-labeled materials for 1 h at 37 °C. The mitochondria were washed with PBS three times to remove unbound materials. Finally, the fluorescence of the mitochondrial suspension was measured using a flow cytometer.

Cell Viability. NPCs were seeded in 96-well plates at 8×10^3 cells per well. After different treatments, CCK8 (Beyotime, China) working solution was prepared by mixing the CCK8 solution with serum-free 1:9 according to the reagent manufacturer's instructions and incubated with the cells in a 37 °C incubator in the dark for 2 h. The absorbance was finally observed at 450 nm.

https://doi.org/10.1021/acsnano.3c12163
ACS Nano 2024, 18, 8885−8905

Cytosolic ROS and Mitochondrial ROS Scavenging Efficiency. The NPCs were seeded in 96-well plates, with 8×10^3 cells in each well. After the cells were completely attached, they were treated with H_2O_2 (100 mM) for 30 min, then PBS, PGA-Mn, and PGA-Mn-TP04 were added, and incubated for 12 h. The DCFH-DA (Beyotime, China) and Mito-Sox (Yeasen Biotechnology, China) were added to detect cROS and mROS according to the reagent manufacturer's instructions, and after 20 min of incubation in a 37 °C incubator in the dark, the excess dye was washed with PBS three times. This was followed by observation with an inverted fluorescence microscope (Carl Zeiss Inc., Zeiss Axiovert A1, USA).

Cell Apoptosis and Necrosis. NPCs were collected according to the instructions of the reagent manufacturer and gently blown to the single cell suspension with 100 μL 1 × Binding Buffer, and then, 5 μL Annexin V-FITC and 5 μL PI Staining Solution (Vazyme Biotech, China) were added. The cells were incubated in the dark at room temperature (20−25 °C) for 10 min, and then, 400 μL of 1 × Binding Buffer was added and gently mixed. Finally, CytoFLEX (Beckman Coulter WM2016014, USA) was used to analyze the apoptosis and necrosis rate of the cells.

ATP Content Detection. NPCs were seeded in 6-well plates at 1×10^5 cells per well, and the cells were treated with different treatments after the cells were completely attached to the well. Cells were subsequently lysed according to the reagent manufacturer's instructions. 200 μL of lysate was added to each well, and after lysis, the supernatant was removed by centrifugation at 12 000*g* for 5 min at 4 °C. Samples were detected by adding 100 μM ATP to the working solution (Vazyme Biotech, China). After 5 min at room temperature, the samples were tested for fluorescence intensity using a chemiluminescence apparatus.

Detection of Mitochondrial Membrane Potential. NPCs were seeded in a 96-well plate at 8×10^3 cells per well, and the cells were treated with different treatments after the cells were completely adherent. The cells were then incubated with 5 μM JC-1 (C2006 Beyotime, China) reagent for 20 min at 37 °C ambient protected from light and then washed twice after precooling using the buffer provided in the kit. The red-to-green ratio was observed under a fluorescent microscope in response to changes in membrane potential.

Mitochondrial Structure Observation. The NPCs were collected using trypsin, and the cells were fixed with electron microscope fixative (Servicebio G1102). The cells were fixed in 0.1 M phosphate buffer containing 1% osmium tetroxide (Ted Pella Inc. 18456). The cells were subsequently dehydrated in a graded ethanol series and subsequently embedded. Sections were made at a thickness of 60−80 nm in an ultrathin sectioning machine. Sections were poststained with dicumyl acetate and lead citrate and used for TEM (HITACHI HT7700, Japan).

Immunofluorescence Staining. NPCs were seeded in 12-well plates, and NPCs were treated with different treatments after they were completely adherent. After 12 h, the cells were fixed with 4% paraformaldehyde for 15 min and permeabilized with 0.1% Triton for 5 min. After blocking with 10% goat serum for 1 h, the cells were incubated with 1:400 diluted primary antibodies (MMP13 (Abcam, USA), COL2A1(Abcam, USA) overnight. Then, after washing with PBS, the cells were incubated with secondary antibodies for 2 h at room temperature and finally visualized by an inverted microscope and semiquantitative analysis using ImageJ.

Western Blot. NPCs were lysed on ice with RIPA lysate buffer (Beyotime, China) containing 1 mM PMSF (Beyotime, China). Total protein in the lysate was then extracted in a 4 °C centrifuge at 12 000 rpm, and sample protein concentrations were determined using a BCA protein analysis kit (Beyotime, China). Equal amounts of target proteins were isolated from each sample using 8−12% SDS-PAGE gels (Vazyme Biotech, China) and transferred to PVDF membranes (Bio-Rad, Hercules, CA, USA). The samples were blocked for 15 min at room temperature with Rapid Blocking Solution (Beyotime, China) and then incubated overnight at 4 °C in a refrigerator with the following primary antibodies: Aggrecan (1:1000), ADMAST (1:1000), COL2A1 (1:1000), MMP13 (1:1000), Drp1(1:1000), MFN1 (1:1000), MFN2 (1:1000), OPA1 (1:1000) After washing with PBS, the samples were incubated with the corresponding secondary antibodies for 2 h at room temperature, and the bands were detected with ECL luminescence reagents and analyzed by ImageJ.

qRT-PCR for RNA Expression Level. Total RNA was extracted from NPCs using the total RNA extraction kit (Beyotime, China), and then, RNA was converted to cDNA using the PrimeScript RT kit (Takara, Japan). RT-PCR was performed using the TB green qRT-PCR kit (Takara, Japan) and a two-step RT-PCR system (LightCycler 96, Germany). The primer sequences are shown in Table S5.

Animal Experimental Details. SD rats (male, 6 weeks old) were purchased from the Experimental Animal Center of Zhejiang Province, with the ethical approval of Experimental Animal Ethics Committee of Wenzhou Institute, University of Chinese Academy of Sciences (ID Number: xmsq2022−0064). The rats were divided into four groups: control, IVDD, PGA-Mn, and PGA-Mn-TP04. After anesthesia with 2% (w/v) pentobarbital (40 mg/kg), the caudal vertebra was punctured vertically with a 27 G needle (Co 7/8) at a fixed depth of 4 mm and held for 1 min. Then, 10 μL of the material (PBS, PGA-Mn (50 μM), PGA-Mn-TP04 (50 μM)) was injected into the IVD with a micro syringe.

X-ray and MRI Examination. At 4 and 8 weeks after surgery, three rats were randomly selected from each group, and rats were anesthetized by intraperitoneal injection of 10% pentobarbital (40 mg/kg). Then, rats were maintained in a prone position for X-ray and MRI examination. X-ray exposure parameters were 50 Kv and 160 μA. MRI images of rat tails were taken by 3.0 T MRI (Philips Intera Achieva 3.0 MR, USA) to evaluate the signal and structural changes of IVD. The degree of IVDD was evaluated by three orthopedic investigators using the Pfirrmann and DHI grading systems on MRI and X-ray.

Histological Analysis. At 4 and 8 weeks after surgery, the rats were sacrificed, and IVDs were collected. After being fixed with 4% para-formaldehyde for a day, the samples were decalcified with 10% EDTA for one month. The samples were then embedded in paraffin and cut into 5 μm histological sections containing end plate, AF, and NP. The IVD structural changes were observed by Hematoxylin and Eosin (HE), Safranin-O/Fast Green (SF), and immunohistochemistry (IHC). Histological grades were calculated based on existing studies (Table S3).[80] The relative positive rate of IHC was analyzed by ImageJ.

RNA-seq and Data Analysis. Total RNA was isolated from each thymus sample using the RNAmini kit (Qiagen, Germany). RNA quality was determined by gel electrophoresis and qubits (Thermo, Waltham, MA, USA). Only high-quality RNA samples (OD260/280 = 1.8−2.2, OD260/230 ≥ 2.0, RIN ≥ 6.5, 28S:18S ≥ 1.0, > 2 μg) were used to construct sequencing libraries. Strk-specific libraries were constructed using the TruSeq RNA sample Preparation Kit (Illumina, San Diego, CA, USA) and sequenced using an Illumina Novaseq 6000 sequencer. Raw data are provided by FastQC v0.11.2 software was used to check the quality of the data.

Statistical Analysis. All assays in this work were performed in at least three independent experiments. Statistical analyses were performed using Prism 9 (GraphPad Software, USA) and are expressed as mean ± standard deviation (mean ± SD). Comparisons between more than two groups were performed using ANOVA and Bonferroni test. Values of $P < 0.05$ were considered statistically significant, with increased confidence levels shown as $^*P < 0.05$, $^{**}P < 0.01$, $^{***}P < 0.001$, and $^{****}P < 0.0001$; #$p < 0.05$, ##$p < 0.01$, ###$p < 0.001$, ####$p < 0.0001$.

ASSOCIATED CONTENT

Supporting Information

The Supporting Information is available free of charge at https://pubs.acs.org/doi/10.1021/acsnano.3c12163.

SEM of PGA-Mn-TP04; XRD spectra of GA, PGA; FTIR spectra of GA, PGA, TP04; High-resolution XPS spectra of PGA for C 1s, O 1s and PGA-Mn reacted with ·OH, $\cdot O_2^-$, and H_2O_2; Stability of PGA-Mn-TP04;

https://doi.org/10.1021/acsnano.3c12163
ACS Nano 2024, 18, 8885−8905

Scavenging efficiency of GA, PGA, and PGA-Mn on different ROS; Mn^{3+}(1)-GA(4) and Mn^{3+}(3)-GA(7) model, population analyses; Molecular orbital functions of GA-Mn; Molecular structures of gallate and its one-electron oxidation products; Cyclic voltammograms; Biocompatibility of PGA-Mn and PGA-Mn-TP04; Endocytosis efficiency, Lysosomal escape efficiency, Mitochondrial targeting efficiency of nanoparticles; pH-buffering capacity of nanoparticles; Intraoperative picture of modeling; Live fluorescence imaging; Schematic diagram of measurement used to calculate DHI; Characteristic absorption peak of FITC-labeled TP04; ICP-MS analysis of PGA-Mn; DLS of nanoparticles and characterization of their polydispersibility index; Histologic grading scale; Primers used in quantitative real-time PCR; GPC data of PGA-Mn and PGA-Mn+ROS (PDF)

AUTHOR INFORMATION

Corresponding Authors

Aimin Wu − *Department of Orthopaedics, Key Laboratory of Structural Malformations in Children of Zhejiang Province, Key Laboratory of Orthopaedics of Zhejiang Province, The Second Affiliated Hospital and Yuying Children's Hospital of Wenzhou Medical University, Wenzhou, Zhejiang 325000, China*; Email: aiminwu@wmu.edu.cn

Yunlong Zhou − *Zhejiang Engineering Research Center for Tissue Repair Materials, Wenzhou Institute, University of Chinese Academy of Sciences, Wenzhou, Zhejiang 325000, China*; orcid.org/0000-0001-5654-1170; Email: zhouyl@ucas.ac.cn

Shengwei Jin − *Key Laboratory of Anesthesiology of Zhejiang Province, Wenzhou Medical University, Wenzhou, Zhejiang 325000, China*; Email: jinshengwei69@163.com

Authors

Qizhu Chen − *Department of Orthopaedics, Key Laboratory of Structural Malformations in Children of Zhejiang Province, Key Laboratory of Orthopaedics of Zhejiang Province, The Second Affiliated Hospital and Yuying Children's Hospital of Wenzhou Medical University, Wenzhou, Zhejiang 325000, China*; orcid.org/0009-0007-0206-2167

Qiuping Qian − *Zhejiang Engineering Research Center for Tissue Repair Materials, Wenzhou Institute, University of Chinese Academy of Sciences, Wenzhou, Zhejiang 325000, China*

Hongbo Xu − *Key Laboratory of Anesthesiology of Zhejiang Province, Wenzhou Medical University, Wenzhou, Zhejiang 325000, China*

Hao Zhou − *Department of Orthopaedics, Key Laboratory of Structural Malformations in Children of Zhejiang Province, Key Laboratory of Orthopaedics of Zhejiang Province, The Second Affiliated Hospital and Yuying Children's Hospital of Wenzhou Medical University, Wenzhou, Zhejiang 325000, China*

Linjie Chen − *Department of Orthopaedics, Key Laboratory of Structural Malformations in Children of Zhejiang Province, Key Laboratory of Orthopaedics of Zhejiang Province, The Second Affiliated Hospital and Yuying Children's Hospital of Wenzhou Medical University, Wenzhou, Zhejiang 325000, China*

Nannan Shao − *Zhejiang Engineering Research Center for Tissue Repair Materials, Wenzhou Institute, University of Chinese Academy of Sciences, Wenzhou, Zhejiang 325000, China*

Kai Zhang − *Ninth People's Hospital, Department of Orthopaedics, Shanghai Key Laboratory of Orthopaedic Implants, Shanghai Jiaotong University School of Medicine, Shanghai 200011, China*

Tao Chen − *Department of Orthopaedics, Key Laboratory of Structural Malformations in Children of Zhejiang Province, Key Laboratory of Orthopaedics of Zhejiang Province, The Second Affiliated Hospital and Yuying Children's Hospital of Wenzhou Medical University, Wenzhou, Zhejiang 325000, China*

Haijun Tian − *Department of Orthopaedic Surgery, Shanghai Sixth People's Hospital Affiliated to Shanghai Jiao Tong University School of Medicine, Shanghai 200025, China*

Zhiguang Zhang − *Department of Orthopaedics, Key Laboratory of Structural Malformations in Children of Zhejiang Province, Key Laboratory of Orthopaedics of Zhejiang Province, The Second Affiliated Hospital and Yuying Children's Hospital of Wenzhou Medical University, Wenzhou, Zhejiang 325000, China*

Morgan Jones − *Spine Unit, The Royal Orthopaedic Hospital, Birmingham B31 2AP, U.K.*

Kenny Yat Hong Kwan − *Department of Orthopaedics and Traumatology, Li Ka Shing Faculty of Medicine, The University of Hong Kong, Hong Kong SAR, China*

Mathew Sewell − *Spine Unit, The Royal Orthopaedic Hospital, Birmingham B31 2AP, U.K.*

Shuying Shen − *Department of Orthopaedics, Key Laboratory of Musculoskeletal System Degeneration and Regeneration Translational Research of Zhejiang Province, Sir Run Shaw Hospital, Zhejiang University School of Medicine, Hangzhou, Zhejiang 310013, China*

Xiangyang Wang − *Department of Orthopaedics, Key Laboratory of Structural Malformations in Children of Zhejiang Province, Key Laboratory of Orthopaedics of Zhejiang Province, The Second Affiliated Hospital and Yuying Children's Hospital of Wenzhou Medical University, Wenzhou, Zhejiang 325000, China*

Moonis Ali Khan − *Chemistry Department, College of Science, King Saud University, Riyadh 11451, Saudi Arabia*; orcid.org/0000-0002-0548-8581

Pooyan Makvandi − *The Quzhou Affiliated Hospital of Wenzhou Medical University, Quzhou People's Hospital, Quzhou 324000 Zhejiang, China; Centre of Research Impact and Outcome, Chitkara University, Rajpura 140401 Punjab, India; Department of Biomaterials, Saveetha Dental College and Hospitals, SIMATS, Saveetha University, Chennai 600077, India*

Complete contact information is available at: https://pubs.acs.org/10.1021/acsnano.3c12163

Author Contributions

□These authors (Qizhu Chen, Qiuping Qian, Hongbo Xu, Hao Zhou) contributed equally. Conceptualization: Aimin Wu, Yunlong Zhou, Qiuping Qian. Methodology: Qizhu Chen, Kai Zhang, Hao Zhou, Haijun Tian, Hongbo Xu, Linjie Chen, Tao Chen, Nannan Shao. Investigation: Zhiguang Zhang, Mathew Sewell, Morgan Jones, Kenny Yat Hong Kwan, Shuying Shen, Qizhu Chen. Visualization: Mathew Sewell, Xiangyang Wang,

https://doi.org/10.1021/acsnano.3c12163
ACS Nano 2024, 18, 8885−8905

Qizhu Chen. Supervision: Yunlong Zhou, Shengwei Jin, Aimin Wu. Writing—original draft: Qizhu Chen, Qiuping Qian. Writing—review and editing: Moonis Ali Khan, Pooyan Makvandi, Aimin Wu, Yunlong Zhou, Shengwei Jin.

Notes

The authors declare no competing financial interest.
Some of the diagrams were created with BioRender.com.

ACKNOWLEDGMENTS

Aimin Wu was supported by National Natural Science Foundation of China (82272555), Wenzhou Major Scientific and Technological Innovation Project (ZY2022010), Zhejiang Provincial Natural Science Foundation of China (LGF21H060010), Zhejiang Provincial Medical Technology Foundation of China (2022PY071). Yunlong Zhou greatly acknowledges the financial support from Key Laboratory of Structural Malformations in Children of Zhejiang Province (ZJET2304Z), the National Natural Science Foundation of China (Grant No. 21773172), WIUCASQD2019001, the Research Center of Clinical Functional Materials and Diagnosis & Treatment Devices of Zhejiang Province (WIBEK181006), "Pioneer" and "Leading Goose" R&D Program of Zhejiang (2023C03084), and Wenzhou high-level innovation team (Development and application team of functional liver cancer-on-a-chip) Major Science and Technology Project of Wenzhou Science and Technology (ZG2022017). Moonis Ali Khan acknowledges the financial support through Researchers Supporting Project number (RSP2024R345), King Saud University, Riyadh, Saudi Arabia.

REFERENCES

(1) Maher, C.; Underwood, M.; Buchbinder, R. Non-specific low back pain. *Lancet* **2017**, *389* (10070), 736−747.
(2) Wu, A.; Dong, W.; Liu, S.; Cheung, J. P. Y.; Kwan, K. Y. H.; Zeng, X.; Zhang, K.; Sun, Z.; Wang, X.; Cheung, K. M. C.; Zhou, M.; Zhao, J. The prevalence and years lived with disability caused by low back pain in China, 1990 to 2016: findings from the global burden of disease study 2016. *Pain* **2019**, *160* (1), 237−245.
(3) Urban, J. P.; Roberts, S. Degeneration of the intervertebral disc. *Arthritis Res. Ther* **2003**, *5* (3), 120−30.
(4) Andersson, G. B. Epidemiological features of chronic low-back pain. *Lancet* **1999**, *354* (9178), 581−5.
(5) Deyo, R. A.; Mirza, S. K. CLINICAL PRACTICE. Herniated Lumbar Intervertebral Disk. *N Engl J. Med.* **2016**, *374* (18), 1763−72.
(6) Global Burden of Disease Study 2013 Collaborators. Global, regional, and national incidence, prevalence, and years lived with disability for 301 acute and chronic diseases and injuries in 188 countries, 1990−2013: a systematic analysis for the Global Burden of Disease Study 2013. *Lancet* **2015**, *386* (9995), 743−800.
(7) Priyadarshani, P.; Li, Y.; Yao, L. Advances in biological therapy for nucleus pulposus regeneration. *Osteoarthritis Cartilage* **2016**, *24* (2), 206−12.
(8) Li, G.; Ma, L.; He, S.; Luo, R.; Wang, B.; Zhang, W.; Song, Y.; Liao, Z.; Ke, W.; Xiang, Q.; Feng, X.; Wu, X.; Zhang, Y.; Wang, K.; Yang, C. WTAP-mediated m(6)A modification of lncRNA NORAD promotes intervertebral disc degeneration. *Nat. Commun.* **2022**, *13* (1), 1469.
(9) Silagi, E. S.; Shapiro, I. M.; Risbud, M. V. Glycosaminoglycan synthesis in the nucleus pulposus: Dysregulation and the pathogenesis of disc degeneration. *Matrix Biol.* **2018**, *71*−*72*, 368−379.
(10) Li, B. L.; Liu, X.; Gao, M.; Zhang, F.; Chen, X.; He, Z.; Wang, J.; Tian, W.; Chen, D.; Zhou, Z.; Liu, S. Programmed NP Cell Death Induced by Mitochondrial ROS in a One-Strike Loading Disc Degeneration Organ Culture Model. *Oxid Med. Cell Longev* **2021**, *2021*, 5608133.
(11) Song, Y.; Lu, S.; Geng, W.; Feng, X.; Luo, R.; Li, G.; Yang, C. Mitochondrial quality control in intervertebral disc degeneration. *Exp Mol. Med.* **2021**, *53* (7), 1124−1133.
(12) Lin, Z.; Wang, H.; Song, J.; Xu, G.; Lu, F.; Ma, X.; Xia, X.; Jiang, J.; Zou, F. The role of mitochondrial fission in intervertebral disc degeneration. *Osteoarthritis Cartilage* **2023**, *31* (2), 158−166.
(13) Binch, A. L. A.; Fitzgerald, J. C.; Growney, E. A.; Barry, F. Cell-based strategies for IVD repair: clinical progress and translational obstacles. *Nat. Rev. Rheumatol* **2021**, *17* (3), 158−175.
(14) Liu, W.; Ma, Z.; Wang, Y.; Yang, J. Multiple nano-drug delivery systems for intervertebral disc degeneration: Current status and future perspectives. *Bioact Mater.* **2023**, *23*, 274−299.
(15) Li, Z.; Lang, G.; Chen, X.; Sacks, H.; Mantzur, C.; Tropp, U.; Mader, K. T.; Smallwood, T. C.; Sammon, C.; Richards, R. G.; Alini, M.; Grad, S. Polyurethane scaffold with in situ swelling capacity for nucleus pulposus replacement. *Biomaterials* **2016**, *84*, 196−209.
(16) Blanquer, S. B.; Grijpma, D. W.; Poot, A. A. Delivery systems for the treatment of degenerated intervertebral discs. *Adv. Drug Deliv Rev.* **2015**, *84*, 172−87.
(17) Feng, G.; Chen, H.; Li, J.; Huang, Q.; Gupte, M. J.; Liu, H.; Song, Y.; Ge, Z. Gene therapy for nucleus pulposus regeneration by heme oxygenase-1 plasmid DNA carried by mixed polyplex micelles with thermo-responsive heterogeneous coronas. *Biomaterials* **2015**, *52*, 1−13.
(18) Li, J.; Chen, Q.; Zha, Z.; Li, H.; Toh, K.; Dirisala, A.; Matsumoto, Y.; Osada, K.; Kataoka, K.; Ge, Z. Ternary polyplex micelles with PEG shells and intermediate barrier to complexed DNA cores for efficient systemic gene delivery. *J. Controlled Release* **2015**, *209*, 77−87.
(19) Chen, Z.; Lv, Z.; Zhuang, Y.; Saiding, Q.; Yang, W.; Xiong, W.; Zhang, Z.; Chen, H.; Cui, W.; Zhang, Y. Mechanical Signal-Tailored Hydrogel Microspheres Recruit and Train Stem Cells for Precise Differentiation. *Adv. Mater.* **2023**, *35* (40), No. e2300180.
(20) Song, C.; Xu, Y.; Peng, Q.; Chen, R.; Zhou, D.; Cheng, K.; Cai, W.; Liu, T.; Huang, C.; Fu, Z.; Wei, C.; Liu, Z. Mitochondrial dysfunction: a new molecular mechanism of intervertebral disc degeneration. *Inflamm Res.* **2023**, *72* (12), 2249−2260.
(21) Ni, H. M.; Williams, J. A.; Ding, W. X. Mitochondrial dynamics and mitochondrial quality control. *Redox Biol.* **2015**, *4*, 6−13.
(22) Heinke, L. Mitochondrial ROS drive cell cycle progression. *Nat. Rev. Mol. Cell Biol.* **2022**, *23* (9), 581.
(23) Spinelli, J. B.; Haigis, M. C. The multifaceted contributions of mitochondria to cellular metabolism. *Nat. Cell Biol.* **2018**, *20* (7), 745−754.
(24) Giacomello, M.; Pyakurel, A.; Glytsou, C.; Scorrano, L. The cell biology of mitochondrial membrane dynamics. *Nat. Rev. Mol. Cell Biol.* **2020**, *21* (4), 204−224.
(25) Tsushima, K.; Bugger, H.; Wende, A. R.; Soto, J.; Jenson, G. A.; Tor, A. R.; McGlauflin, R.; Kenny, H. C.; Zhang, Y.; Souvenir, R.; Hu, X. X.; Sloan, C. L.; Pereira, R. O.; Lira, V. A.; Spitzer, K. W.; Sharp, T. L.; Shoghi, K. I.; Sparagna, G. C.; Rog-Zielinska, E. A.; Kohl, P.; et al. Mitochondrial Reactive Oxygen Species in Lipotoxic Hearts Induce Post-Translational Modifications of AKAP121, DRP1, and OPA1 That Promote Mitochondrial Fission. *Circ. Res.* **2018**, *122* (1), 58−73.
(26) Zorov, D. B.; Juhaszova, M.; Sollott, S. J. Mitochondrial reactive oxygen species (ROS) and ROS-induced ROS release. *Physiol Rev.* **2014**, *94* (3), 909−50.
(27) Lee, W. M.; Kaplowitz, N. Alcohol, Fasting, and Therapeutic Dosing of Acetaminophen: A Perfect Storm. *Hepatology* **2021**, *73* (5), 1634−1636.
(28) Yan, R.; Ren, J.; Wen, J.; Cao, Z.; Wu, D.; Qin, M.; Xu, D.; Castillo, R.; Li, F.; Wang, F.; Gan, Z.; Liu, C.; Wei, P.; Lu, Y. Enzyme Therapeutic for Ischemia and Reperfusion Injury in Organ Transplantation. *Adv. Mater.* **2022**, *34* (1), No. e2105670.
(29) Wang, T.; Fan, Q.; Hong, J.; Chen, Z.; Zhou, X.; Zhang, J.; Dai, Y.; Jiang, H.; Gu, Z.; Cheng, Y.; Li, Y. Therapeutic Nanoparticles from Grape Seed for Modulating Oxidative Stress. *Small* **2021**, *17* (45), No. e2102485.

https://doi.org/10.1021/acsnano.3c12163
ACS Nano 2024, 18, 8885−8905

(30) Chen, Y.; Luo, R.; Li, J.; Wang, S.; Ding, J.; Zhao, K.; Lu, B.; Zhou, W. Intrinsic Radical Species Scavenging Activities of Tea Polyphenols Nanoparticles Block Pyroptosis in Endotoxin-Induced Sepsis. *ACS Nano* **2022**, *16* (2), 2429−2441.
(31) Zhang, T.; Wang, Y.; Li, R.; Xin, J.; Zheng, Z.; Zhang, X.; Xiao, C.; Zhang, S. ROS-responsive magnesium-containing microspheres for antioxidative treatment of intervertebral disc degeneration. *Acta Biomater* **2023**, *158*, 475−492.
(32) Zhou, T.; Yang, X.; Chen, Z.; Yang, Y.; Wang, X.; Cao, X.; Chen, C.; Han, C.; Tian, H.; Qin, A.; Fu, J.; Zhao, J. Prussian Blue Nanoparticles Stabilize SOD1 from Ubiquitination-Proteasome Degradation to Rescue Intervertebral Disc Degeneration. *Adv. Sci. (Weinh)* **2022**, *9* (10), No. e2105466.
(33) Zhang, S.; Gao, H.; Bao, G. Physical Principles of Nanoparticle Cellular Endocytosis. *ACS Nano* **2015**, *9* (9), 8655−71.
(34) Stewart, M. P.; Sharei, A.; Ding, X.; Sahay, G.; Langer, R.; Jensen, K. F. In vitro and ex vivo strategies for intracellular delivery. *Nature* **2016**, *538* (7624), 183−192.
(35) Behzadi, S.; Serpooshan, V.; Tao, W.; Hamaly, M. A.; Alkawareek, M. Y.; Dreaden, E. C.; Brown, D.; Alkilany, A. M.; Farokhzad, O. C.; Mahmoudi, M. Cellular uptake of nanoparticles: journey inside the cell. *Chem. Soc. Rev.* **2017**, *46* (14), 4218−4244.
(36) Zielonka, J.; Joseph, J.; Sikora, A.; Hardy, M.; Ouari, O.; Vasquez-Vivar, J.; Cheng, G.; Lopez, M.; Kalyanaraman, B. Mitochondria-Targeted Triphenylphosphonium-Based Compounds: Syntheses, Mechanisms of Action, and Therapeutic and Diagnostic Applications. *Chem. Rev.* **2017**, *117* (15), 10043−10120.
(37) Zhang, Y.; Khalique, A.; Du, X.; Gao, Z.; Wu, J.; Zhang, X.; Zhang, R.; Sun, Z.; Liu, Q.; Xu, Z.; Midgley, A. C.; Wang, L.; Yan, X.; Zhuang, J.; Kong, D.; Huang, X. Biomimetic Design of Mitochondria-Targeted Hybrid Nanozymes as Superoxide Scavengers. *Adv. Mater.* **2021**, *33* (9), No. e2006570.
(38) Zhang, J.; Gao, B.; Ye, B.; Sun, Z.; Qian, Z.; Yu, L.; Bi, Y.; Ma, L.; Ding, Y.; Du, Y.; Wang, W.; Mao, Z. Mitochondrial-Targeted Delivery of Polyphenol-Mediated Antioxidases Complexes against Pyroptosis and Inflammatory Diseases. *Adv. Mater.* **2023**, *35* (11), No. e2208571.
(39) Wang, X.; Lei, Y.; Jiang, K.; Yan, C.; Shen, J.; Zhao, W.; Xiang, C.; Cai, Z.; Song, Y.; Chen, L.; et al. Mito-battery: Micro-nanohydrogel microspheres for targeted regulation of cellular mitochondrial respiratory chain. *Nano Today* **2023**, *49*, 101820.
(40) Davinelli, S.; De Stefani, D.; De Vivo, I.; Scapagnini, G. Polyphenols as Caloric Restriction Mimetics Regulating Mitochondrial Biogenesis and Mitophagy. *Trends Endocrinol Metab* **2020**, *31* (7), 536−550.
(41) Badhani, B.; Sharma, N.; Kakkar, R. Gallic acid: a versatile antioxidant with promising therapeutic and industrial applications. *RSC Adv.* **2015**, *5* (35), 27540−27557.
(42) Jomova, K.; Makova, M.; Alomar, S. Y.; Alwasel, S. H.; Nepovimova, E.; Kuca, K.; Rhodes, C. J.; Valko, M. Essential metals in health and disease. *Chem. Biol. Interact* **2022**, *367*, 110173.
(43) Liu, M.; Sun, X.; Chen, B.; Dai, R.; Xi, Z.; Xu, H. Insights into Manganese Superoxide Dismutase and Human Diseases. *Int. J. Mol. Sci.* **2022**, *23* (24), 15893.
(44) Wei, Z.; Fan, Z.; Peng, G.; Si, H.; Yang, L.; Wang, Z.; Yin, S.; Chen, S.; Wang, R.; Xie, Y.; Zhao, C. Extracorporeal hemoperfusion therapy for sepsis: Multi-lamellar microspheres towards cascade endotoxin removal and broad-spectrum radical eliminating. *Chemical Engineering Journal* **2022**, *444*, 136499.
(45) Zaccaron, S.; Ganzerla, R.; Bortoluzzi, M. Iron complexes with gallic acid: a computational study on coordination compounds of interest for the preservation of cultural heritage. *J. Coord. Chem.* **2013**, *66* (10), 1709−1719.
(46) Yang, B.; Yao, H.; Tian, H.; Yu, Z.; Guo, Y.; Wang, Y.; Yang, J.; Chen, C.; Shi, J. Intratumoral synthesis of nano-metalchelate for tumor catalytic therapy by ligand field-enhanced coordination. *Nat. Commun.* **2021**, *12* (1), 3393.
(47) Pardeshi, S.; Dhodapkar, R.; Kumar, A. Quantum chemical density functional theory studies on the molecular structure and vibrational spectra of Gallic acid imprinted polymers. *Spectrochim Acta A Mol. Biomol Spectrosc* **2013**, *116*, 562−73.
(48) Rajan, V. K.; Muraleedharan, K. A computational investigation on the structure, global parameters and antioxidant capacity of a polyphenol, Gallic acid. *Food Chem.* **2017**, *220*, 93−99.
(49) Leopoldini, M.; Russo, N.; Toscano, M. The molecular basis of working mechanism of natural polyphenolic antioxidants. *Food chemistry* **2011**, *125* (2), 288−306.
(50) Daouda, D.; Douadi, T.; Ghobrini, D.; Lahouel, N.; Hamani, H. Investigation of some phenolic-type antioxidants compounds extracted from biodiesel as green natural corrosion inhibitors; DFT and molecular dynamic simulation, comparative study. *AIP Conference Proceedings* **2019**, *2190*, 020098.
(51) Abdel-Hamid, R.; Newair, E. F. Electrochemical behavior of antioxidants: I. Mechanistic study on electrochemical oxidation of gallic acid in aqueous solutions at glassy-carbon electrode. *J. Electroanal. Chem.* **2011**, *657* (1−2), 107−112.
(52) Reed, A. E.; Curtiss, L. A.; Weinhold, F. Intermolecular interactions from a natural bond orbital, donor-acceptor viewpoint. *Chem. Rev.* **1988**, *88* (6), 899−926.
(53) Perron, N. R.; Wang, H. C.; DeGuire, S. N.; Jenkins, M.; Lawson, M.; Brumaghim, J. L. Kinetics of iron oxidation upon polyphenol binding. *Dalton Transactions* **2010**, *39* (41), 9982−9987.
(54) Hage, R.; Iburg, J. E.; Kerschner, J.; Koek, J. H.; Lempers, E. L. M.; Martens, R. J.; Racherla, U. S.; Russell, S. W.; Swarthoff, T.; van Vliet, M. R. P.; Warnaar, J. B.; Wolf, L. v. d.; Krijnen, B. Efficient manganese catalysts for low-temperature bleaching. *Nature* **1994**, *369* (6482), 637−639.
(55) Schlosser, D.; Höfer, C. Laccase-catalyzed oxidation of Mn2+ in the presence of natural Mn3+ chelators as a novel source of extracellular H2O2 production and its impact on manganese peroxidase. *Appl. Environ. Microbiol.* **2002**, *68* (7), 3514−3521.
(56) Yamada, Y.; Satrialdi; Hibino, M.; Sasaki, D.; Abe, J.; Harashima, H. Power of mitochondrial drug delivery systems to produce innovative nanomedicines. *Adv. Drug Deliv Rev.* **2020**, *154*−*155*, 187−209.
(57) Chen, J.; Li, J.; Zhou, J.; Lin, Z.; Cavalieri, F.; Czuba-Wojnilowicz, E.; Hu, Y.; Glab, A.; Ju, Y.; Richardson, J. J.; Caruso, F. Metal-Phenolic Coatings as a Platform to Trigger Endosomal Escape of Nanoparticles. *ACS Nano* **2019**, *13* (10), 11653−11664.
(58) Voltà-Durán, E.; Parladé, E.; Serna, N.; Villaverde, A.; Vazquez, E.; Unzueta, U. Endosomal escape for cell-targeted proteins. Going out after going in. *Biotechnol Adv.* **2023**, *63*, 108103.
(59) Wojnilowicz, M.; Glab, A.; Bertucci, A.; Caruso, F.; Cavalieri, F. Super-resolution Imaging of Proton Sponge-Triggered Rupture of Endosomes and Cytosolic Release of Small Interfering RNA. *ACS Nano* **2019**, *13* (1), 187−202.
(60) Hou, T.; Wang, X.; Ma, Q.; Cheng, H. Mitochondrial flashes: new insights into mitochondrial ROS signalling and beyond. *J. Physiol* **2014**, *592* (17), 3703−13.
(61) Zhao, Q.; Liu, J.; Deng, H.; Ma, R.; Liao, J. Y.; Liang, H.; Hu, J.; Li, J.; Guo, Z.; Cai, J.; Xu, X.; Gao, Z.; Su, S. Targeting Mitochondria-Located circRNA SCAR Alleviates NASH via Reducing mROS Output. *Cell* **2020**, *183* (1), 76−93.e22.
(62) Kaminskyy, V. O.; Zhivotovsky, B. Free radicals in cross talk between autophagy and apoptosis. *Antioxid Redox Signal* **2014**, *21* (1), 86−102.
(63) Nunnari, J.; Suomalainen, A. Mitochondria: in sickness and in health. *Cell* **2012**, *148* (6), 1145−59.
(64) Willems, P. H.; Rossignol, R.; Dieteren, C. E.; Murphy, M. P.; Koopman, W. J. Redox Homeostasis and Mitochondrial Dynamics. *Cell Metab* **2015**, *22* (2), 207−18.
(65) Chen, T.; Qian, Q.; Makvandi, P.; Zare, E. N.; Chen, Q.; Chen, L.; Zhang, Z.; Zhou, H.; Zhou, W.; Wang, H.; Wang, X.; Chen, Y.; Zhou, Y.; Wu, A. Engineered high-strength biohydrogel as a multifunctional platform to deliver nucleic acid for ameliorating intervertebral disc degeneration. *Bioactive Materials* **2023**, *25*, 107−121.

https://doi.org/10.1021/acsnano.3c12163
ACS Nano 2024, 18, 8885−8905

(66) Xu, W.; Zhang, X.; Liu, G.; Zhu, M.; Wu, Y.; Jie, Z.; Xie, Z.; Wang, S.; Ma, Q.; Fan, S.; Fang, X. Oxidative stress abrogates the degradation of KMT2D to promote degeneration in nucleus pulposus. *Biochim Biophys Acta Mol. Basis Dis* **2020**, *1866* (10), 165888.
(67) Guo, Q.; Zhu, D.; Wang, Y.; Miao, Z.; Chen, Z.; Lin, Z.; Lin, J.; Huang, C.; Pan, L.; Wang, L.; Zeng, S.; Wang, J.; Zheng, X.; Lin, Y.; Zhang, X.; Wu, Y. Targeting STING attenuates ROS induced intervertebral disc degeneration. *Osteoarthritis Cartilage* **2021**, *29* (8), 1213−1224.
(68) Xu, Y.; Gu, Y.; Cai, F.; Xi, K.; Xin, T.; Tang, J.; Wu, L.; Wang, Z.; Wang, F.; Deng, L.; Pereira, C. L.; Sarmento, B.; Cui, W.; Chen, L. Metabolism Balance Regulation via Antagonist-Functionalized Injectable Microsphere for Nucleus Pulposus Regeneration. *Adv. Funct. Mater.* **2020**, *30* (52), 2006333.
(69) Lee, C.; Yang, W.; Parr, R. G. Development of the Colle-Salvetti correlation-energy formula into a functional of the electron density. *Phys. Rev. B* **1988**, *37* (2), 785−789.
(70) Becke, A. D. Density-functional thermochemistry. III. The role of exact exchange. *J. Chem. Phys.* **1993**, *98* (7), 5648−5652.
(71) Stephens, P. J.; Devlin, F. J.; Chabalowski, C. F.; Frisch, M. J. Ab Initio Calculation of Vibrational Absorption and Circular Dichroism Spectra Using Density Functional Force Fields. *J. Phys. Chem.* **1994**, *98* (45), 11623−11627.
(72) Rassolov, V. A.; Ratner, M. A.; Pople, J. A.; Redfern, P. C.; Curtiss, L. A. 6-31G* basis set for third-row atoms. *J. Comput. Chem.* **2001**, *22* (9), 976−984.
(73) Hay, P. J.; Wadt, W. R. Abinitio Effective Core Potentials for Molecular Calculations - Potentials for K to Au Including the Outermost Core Orbitals. *J. Chem. Phys.* **1985**, *82* (1), 299−310.
(74) Feller, D. The role of databases in support of computational chemistry calculations. *J. Comput. Chem.* **1996**, *17* (13), 1571−1586.
(75) Andrae, D.; Haussermann, U.; Dolg, M.; Stoll, H.; Preuss, H. Energy-adjustedab initio pseudopotentials for the second and third row transition elements: Molecular test for M2 (M = Ag, Au) and MH (M = Ru, Os). *Theor Chim Acta* **1991**, *78* (4), 247−266.
(76) Tomasi, J.; Mennucci, B.; Cammi, R. Quantum mechanical continuum solvation models. *Chem. Rev.* **2005**, *105* (8), 2999−3093.
(77) Lu, T.; Chen, F. Multiwfn: a multifunctional wavefunction analyzer. *J. Comput. Chem.* **2012**, *33* (5), 580−92.
(78) Frisch, M. J.; Trucks, G. W.; Schlegel, H. B.; Scuseria, G. E.; Robb, M. A.; Cheeseman, J. R.; Scalmani, G.; Barone, V.; Mennucci, B.; Petersson, G. A.; Nakatsuji, H.; Caricato, M.; Li, X.; Hratchian, H. P.; Izmaylov, A. F.; Bloino, J.; Zheng, G.; Sonnenberg, J. L.; Hada, M.; Ehara, M.; Toyota, K.; Fukuda, R.; Hasegawa, J.; Ishida, M.; Nakajima, T.; Honda, Y.; Kitao, O.; Nakai, H.; Vreven, T.; Montgomery, J. A., Jr.; Peralta, J. E.; Ogliaro, F.; Bearpark, M.; Heyd, J. J.; Brothers, E.; Kudin, K. N.; Staroverov, V. N.; Kobayashi, R.; Normand, J.; Raghavachari, K.; Rendell, A.; Burant, J. C.; Iyengar, S. S.; Tomasi, J.; Cossi, M.; Rega, N.; Millam, J. M.; Klene, M.; Knox, J. E.; Cross, J. B.; Bakken, V.; Adamo, C.; Jaramillo, J.; Gomperts, R.; Stratmann, R. E.; Yazyev, O.; Austin, A. J.; Cammi, R.; Pomelli, C.; Ochterski, J. W.; Martin, R. L.; Morokuma, K.; Zakrzewski, V. G.; Voth, G. A.; Salvador, P.; Dannenberg, J. J.; Dapprich, S.; Daniels, A. D.; Farkas, O.; Foresman, J. B.; Ortiz, J. V.; Cioslowski, J.; Fox, D. J. *Gaussian 09*, revision B.01; Gaussian, Inc.: Wallingford, CT, 2009.
(79) Legault, C. Y. *CYLview, 1.0b*; Université de Sherbrooke, 2009.
(80) Masuda, K.; Aota, Y.; Muehleman, C.; Imai, Y.; Okuma, M.; Thonar, E. J.; Andersson, G. B.; An, H. S. A novel rabbit model of mild, reproducible disc degeneration by an anulus needle puncture: correlation between the degree of disc injury and radiological and histological appearances of disc degeneration. *Spine (Phila Pa 1976)* **2005**, *30* (1), 5−14.

https://doi.org/10.1021/acsnano.3c12163
ACS Nano 2024, 18, 8885−8905